Q. J. R. Meteorol. Soc. (2006), **132**, pp. 2719–2748 doi: 10.1256/qj.05.162

Microphysical and optical properties of midlatitude cirrus clouds observed in the southern hemisphere during INCA

By JEAN-FRANCOIS GAYET[1]*, VALERY SHCHERBAKOV[2], HERMANN MANNSTEIN[3], ANDEAS MINIKIN[3], ULRICH SCHUMANN[3], JOHAN STRÖM[4], ANDREAS PETZOLD[3], JOELLE OVARLEZ[5] and FRANZ IMMLER[6]

[1]*LaMP, UMR/CNRS no. 6016, Université Blaise Pascal, Clermont-Fd, France*
[2]*Institute of Physics, Minsk, Belarus*
[3]*Institut für Physik der Atmosphäre, DLR, Oberpfaffenhofen, Germany*
[4]*Institute of Applied Environmental Research, Stockholm University, Sweden*
[5]*Laboratoire de Météorologie Dynamique, CNRS/IPSL, Ecole Polytechnique, Palaiseau, France*
[6]*Alfred Wegener Institute for Polar and Marine Research (AWI), Bremerhaven, Germany*

(Received 29 July 2005, revised 9 May 2006)

SUMMARY

Airborne microphysical and optical properties of cirrus clouds, jet-stream and wave clouds were measured at temperatures ranging from −25 °C to −62 °C in the southern hemisphere from Punta Arenas (53°S) in March and April 2000 during the INCA experiment (INterhemispheric differences in Cirrus properties from Anthropogenic emissions). The observations related to cirrus clouds show general decreases of the ice water content (18 mg m^{-3} to 0.05 mg m^{-3}), extinction coefficient (0.70 km^{-1} to 0.08 km^{-1}), ice particle concentration (2.2 cm^{-3} to 0.5 cm^{-3}), and the effective diameter (80 μm to 17 μm) linked to the variation of ambient temperature (−25 °C to −60 °C). The lowest temperature at which supercooled water droplets were detected was −33 °C. The asymmetry parameter shows relatively small variations, with the smallest values (0.758) observed at the lowest temperatures. High-altitude clouds which form with a rapid vertical transport, i.e. jet-stream cirrus and orographic-wave ice-cloud, are characterized by very high values of ice particle concentrations (up to 100 cm^{-3}) compared to mean values as a whole (1.45 cm^{-3}). These two kinds of high clouds are the subjects of detailed case-studies. Although formed at a similar range of temperatures and with similar aerosol properties, the strong differences in cloud properties and humidity fields highlight the key role of the dynamical structure in controlling the formation, evolution and subsequent radiative properties of such high-altitude clouds.

KEYWORDS: Aircraft observations Ice particles Microphysics

1. INTRODUCTION

Cirrus clouds at midlatitudes are important for the atmospheric radiative balance due to their extensive coverage which represents about 20 to 30% of the Earth's surface, according to different observations (Rossow and Schiffer 1999; Wylie and Menzel 1999). The effects of cirrus clouds on visible and infrared radiation are critically determined by microphysical parameters such as ice water content, crystal habit and size distributions (see among others Liou 1986). Since cirrus clouds have a wide variety of physical characteristics (Dowling and Radke 1990), detailed observations form one of the tools that may serve to increase our knowledge of the complex interactions between different physical processes and may serve as a basis for the development of more accurate microphysical and radiative parametrizations for regional and global models.

To a large extent, our knowledge of midlatitude cirrus properties results from several intensive projects carried out mainly in the northern hemisphere, for example FIRE I and FIRE II experiments (e.g. Heymsfield *et al.* 1990; Arnott *et al.* 1994; Heymsfield and Miloshevich 1995) and SUCCESS (Lawson *et al.* 1998) in the USA, or ICE'89 (Raschke *et al.* 1990), EUCREX'94 (Sauvage *et al.* 1999) and AERO-CONTRAIL (Schröder *et al.* 2000) in western Europe. Cirrus cloud microphysical data have been summarized in an overview by Heymsfield and McFarquhar (2002). The distribution of experiments (see Fig. 4.1 in their overview) shows that prior

* Corresponding author: LaMP, Université Blaise Pascale, 24 av. des Landais, 63177 Aubière, France.
e-mail: gayet@opgc.univ-bpclermont.fr

to the INCA (INterhemispheric differences in Cirrus properties from Anthropogenic emissions) experiment (Ström *et al.* 2001) no cirrus study had been performed in southern hemisphere midlatitudes. After INCA, the EMERALD-1 experiment was carried out in South Australia in September 2001 (Gallagher *et al.* 2005).

In this paper we present the results of airborne measurements of microphysical and optical characteristics of high-altitude clouds together with aerosol data obtained during 11 flights performed in the vicinity of Punta Arenas in the south of Chile (53.02°S, 70.86°W) from 23 March to 13 April 2000. The microphysical and optical data were derived from the measurements with PMS FSSP-300, PMS 2D-C and Polar Nephelometer probes. For completeness, we also report interstitial and particle residual aerosol data as obtained from condensation particle counters with heated (250 °C) and unheated inlets, the PMS PCASP-100X aerosol spectrometer probe and the condensation particle counter connected to the counterflow virtual impactor (CVI) inlet. Relative humidity was derived from measurements using a specially designed frost-point hygrometer (Ovarlez *et al.* 2000). These instruments were operated on-board the German DLR (Deutsches Zentrum für Luft- und Raumfahrt) Falcon aircraft. The payload of the aircraft has already been thoroughly described in previous papers (Ovarlez *et al.* 2002; Minikin *et al.* 2003; Seifert *et al.* 2003; Gayet *et al.* 2004). A Mobile Aerosol Raman Lidar (MARL) was also operated by AWI (Alfred Wegener Institute for Polar and Marine Research) at Punta Arenas (Immler and Schrems 2002). In this paper, the instruments used to determine the microphysical and optical properties of cirrus clouds, the analysis procedures, and the prevailing weather and synoptic situation encountered during the field experiment are presented. Thereafter, microphysical and optical properties of all sampled high-altitude clouds, as well as mean aerosol properties, are summarized for different cloud sampling sequences. The results relating to typical cirrus clouds are discussed in terms of mean properties as functions of air temperature and are compared with previous cirrus climatologies. Finally, two case-studies for clouds formed with a rapid vertical transport, i.e. jet-stream cirrus and orographic-wave ice-cloud are presented.

2. Instrumentation and procedures

The instruments used for the determination of microphysical and optical properties of cirrus clouds during INCA have already been thoroughly described in a previous paper (Gayet *et al.* 2004). Three independent techniques are used in this study: (1) the PMS (Particle Measuring System) FSSP-300 (Forward Scattering Spectrometer Probe) operated by the DLR, (2) the PMS 2D-C and (3) the Polar Nephelometer probes, both operated by the LaMP (Laboratoire de Météorologie Physique). The combination of these three techniques provides a description of particles within a diameter range varying from a few micrometres (typically 3 μm) to 800 μm. The method of data processing, the reliability of the instruments and the uncertainties of the derived microphysical and optical parameters have been described in detail by Auriol *et al.* (2001) and Gayet *et al.* (2004).

(*a*) *Microphysical and optical measurements*

In the present study, particles larger than 3 μm diameter were measured by the PMS FSSP-300 optical particle counter (Baumgardner *et al.* 1992). For analysis of the data, the particles are assumed to be ice crystals. The upper size limit of the FSSP-300 in this study is 21.8 μm, which leads to better agreement with the first channels of the 2D-C probe in terms of particle concentration, extinction and ice water content (see below).

The bulk quantities were calculated assuming spherical particles with a density of 0.9 g cm^{-3}.

Controversy remains over whether the high ice-crystal concentrations often reported with the FSSP instrument are real or an artefact, particularly in conditions with lots of large ice crystals (Heymsfield and Miloshevich 1995; Gayet *et al.* 2002a). Indeed, the results of Field *et al*. (2003) suggest that the FSSP concentration may be increased by 2 to 5 times when large ice crystals are present. However, in an earlier analysis of INCA results, Gayet *et al.* (2002a) and Seifert *et al.* (2003) argued that the high concentration of small ice crystals observed during INCA may be considered reliable for a number of reasons. Ice-crystal number concentrations inferred from the FSSP-300 and from residual particle measurement by the Counterflow Virtual Impactor, CVI, (Noone *et al.* 1993) operated onboard the Falcon aircraft during INCA agree rather well (see Fig. 2 in Seifert *et al*. 2003). The hypothesis that the shattering of large ice crystals affects both the FSSP-300 and CVI measurements in the same way appears very unlikely. Indeed, should large ice crystals break up at the CVI inlet it would not be sufficient that small crystals were produced, they would also have to enter the probe, and each crystal would have to leave a residual particle, for the measurements to be thus skewed. Furthermore, the comparison of the extinction derived from the combined dataset of FSSP-300 and 2D-C probes on the one hand, and the Polar Nephelometer (see below) on the other, has shown a consistency between the measurements (Gayet *et al.* 2002a) which would appear unlikely if artefacts dominate the measurements.

In further support of this, we have found cases in the INCA dataset where the relatively high concentration of small ice particles can definitively not be due to shattering effects simply because no ice crystals larger than 100 μm have been observed by the 2D-C probe. We therefore conclude that the effects of ice-crystal shattering on the FSSP data are no greater than the usual random uncertainties (i.e. 75% for a particle concentration of 0.5 cm^{-3}, see Table 1 in Gayet *et al*. (2002a)).

The PMS 2D-C probe provides information on crystal size and shape for the size range 25–800 μm. The method of data processing used in this study has already been described in detail by Gayet *et al.* (2004). We recall that partial images have been rejected from the calculations and the sampling surfaces have been derived accordingly (Heymsfield and Parrish 1978). Even though this leads to a reduction in probe sampling volume, this technique was used rather than the 'reconstructed' method, which allows an extrapolation of the data to particles larger than 800 μm (Heymsfield and Parrish 1978), because (i) the extrapolation may introduce significant additional uncertainties in derived parameters and (ii) ice crystals smaller than 800 μm were the most predominant particles in high-altitude clouds measured during INCA, at least at temperatures below $-35\,^{\circ}$C. The contribution of particles larger than 800 μm to the Ice Water Content (*IWC*) was estimated to be less than 30% for effective diameter larger than 70 μm (preferentially found at warmer temperatures).

In order to improve the statistical significance of low particle concentrations, a 5-second running mean was applied. Irregular ice particles were the most predominant crystals sampled in midlatitude cirrus clouds during INCA. Therefore, the bulk parameters were calculated assuming the surface-equivalent diameter relationships given by Heymsfield (1972) and Locatelli and Hobbs (1974).

As the sensitivity of the probe to small particles decreases with air speed (i.e. $\sim$170 m s^{-1} with the Falcon aircraft), the first six channels (up to 150 μm) were corrected according to the results of Baumgardner and Korolev (1997) assuming that these corrections take into account the miss and/or the undersizing of the particles evidenced by Strapp *et al*. (2001) and by Lawson *et al*. (2006a). The corrections

above were refined by considering interpolations between the FSSP-300 and the 2D-C (in terms of bulk parameters, i.e. extinction coefficient and ice water content) in order to obtain quasi-continuous cumulative probabilities as expected at upper and lower FSSP and 2D-C size limits respectively (i.e. about 20 μm). The use of the first six 2D-C channels was justified, as they were found reliable in terms of statistical significance by applying such statistical procedures as Principal Component Analysis (see Fig. 7 in Shcherbakov *et al.* 2005). Finally, the technique above was validated by comparing the extinctions derived from the PMS probes and the Polar Nephelometer. A noteworthy relationship was found by considering all available data (for south and north INCA experiments) as shown on Fig. 8 in Shcherbakov *et al.* (2005). The slope parameter is found to agree almost perfectly, and the dispersion of the data points falls within the hereafter mentioned uncertainty range.

In the following study, the microphysical parameters were obtained by adding the contributions of the PMS FSSP-300 and 2D-C. The parameter definitions are the following: (i) ice particle concentration (*Conc*), (ii) extinction coefficient (*Ext*), (iii) ice water content (*IWC*) and (iv) effective diameter (*Deff*). This last quantity was calculated, as in earlier studies (Gayet *et al.* 2002a, 2004), using the following relationship:

$$Deff = A\ IWC/Ext \tag{1}$$

with *Deff* expressed in μm, *IWC* in g m^{-3}, *Ext* in km^{-1}, and $A = 3000$ mm^3 g^{-1}.

The accuracy of derived microphysical parameters is considerably affected by inherent shortcomings of probes and data processing. Considering the sampling time of 5 seconds, the total random uncertainties were estimated as ranging from 75% to 100% for PMS probe data (see details in Gayet *et al.* 2002a). These errors may be considerably reduced by taking averages over longer periods.

The Polar Nephelometer (Gayet *et al.* 1997) measures the scattering phase function of an ensemble of cloud particles (i.e. water droplets or ice crystals or a mixture of these particles ranging from a few micrometres to about 800 μm diameter), which intersect a collimated laser beam near the focal point of a parabolic mirror. The light source is a high-power (1.0 W) multimode laser diode operating at $\lambda = 804$ nm. The data acquisition system of the airborne version of the Polar Nephelometer is designed to provide a continuous sampling volume by integrating the measured signals of each of the detectors over a selected period. For instance, the sampling volume (v) is determined by the sampling surface (10 mm long and 5 mm diameter beam) multiplied by the Falcon cruise speed of approximately 170 m s^{-1}, i.e. 850 cm^3 for an acquisition frequency of 10 Hz. This means that the detection threshold is close to one particle per litre at this frequency. Direct measurement of the scattering phase function allows particle types (water droplets or ice crystals) to be distinguished and calculation of the optical parameters to be performed (extinction coefficient and asymmetry parameter, see Gayet *et al.* 2002b).

The Polar Nephelometer provides a more accurate extinction measurement than the PMS probes (accuracy estimated as 25%, see Gayet *et al.* 2002b) because: (i) this measurement provides an integral value, and (ii) statistical errors are considerably reduced. The accuracy of the asymmetry parameter determination is estimated to be within about 4% (Gayet *et al.* 2004).

(*b*) *Clouds sampled and definitions*

Figure 1 shows the research area and the general location of the 11 experimental flights made from Punta Arenas from 23 March to 13 April 2000. The sampling

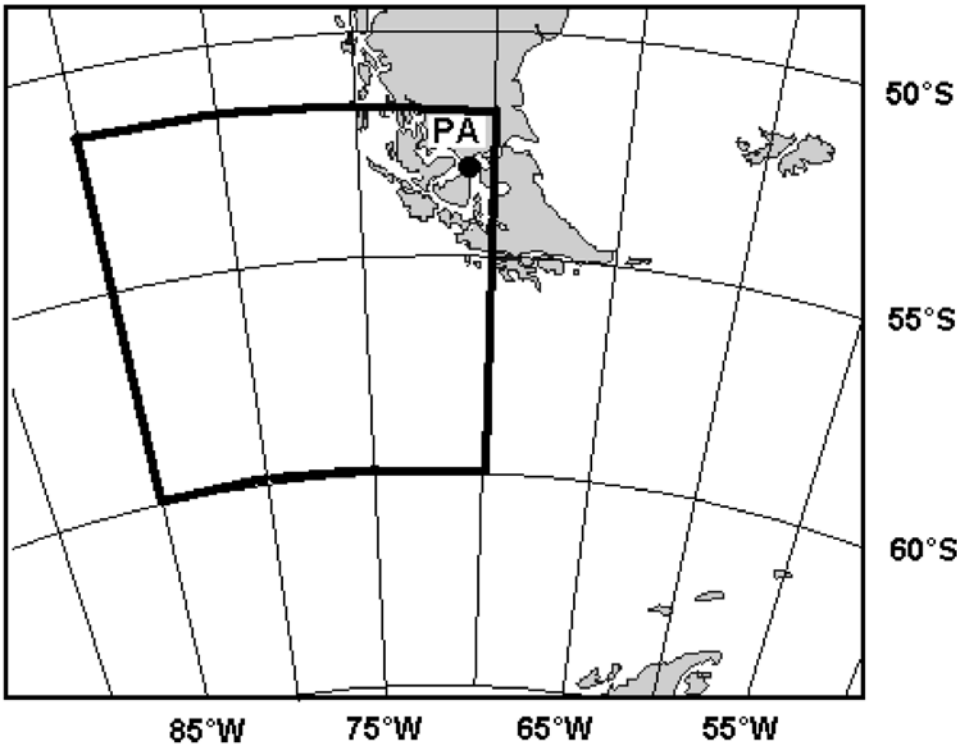

Figure 1. Measurement area and airport of aircraft deployment for the 11 flights made from Punta Arenas (PA) in March and April 2000.

approach has been described elsewhere (Kärcher and Ström 2003). In most cases, the flight patterns consisted of climbing to high altitudes above the main cloud layer and then performing several flight legs at different levels of 10–15 min duration within the cloud. We recall that the Falcon ceiling is about 12 km with the payload used during INCA. The flight legs were mostly oriented perpendicular or parallel to the main wind at cirrus altitude. Several types of high-altitude clouds were sampled, including frontal (cold and warm) cirrus, jet-stream clouds, cirrocumulus, and orographic-wave ice-clouds. We note in passing that the high-altitude clouds observed during INCA were categorized according to the classification by Sassen (2002) which considers optical depths and/or generating mechanism. Table 1 summarizes some characteristics of the sampled clouds and flight patterns. The cloud-top temperatures were estimated at the highest flight level where ice particles were detected. The cloud bases and the cloud types were evaluated from visual observations onboard the aircraft and in post-analysis, and must therefore be considered as rough estimates. The only accurate determinations of the cloud vertical extents were obtained during two flights performed above the AWI Lidar (see Table 1).

In this paper we report average microphysical and optical properties of high-altitude clouds and related aerosols with measurements classified as in-cloud cases when the extinction coefficient values (from the Polar Nephelometer) are higher than the threshold of 0.02 km^{-1}, which roughly corresponds to a concentration of ice particles of 0.1 cm^{-3} with a diameter of 5 μm (FSSP-300 detection limit). Therefore, very small particle concentrations (down to 3×10^{-4} cm^{-3}) evidenced by the CVI during INCA (Kärcher and Ström 2003) were not considered in this study. At the same time, Haag *et al.*

TABLE 1. SOME CHARACTERISTICS OF THE SAMPLED CLOUDS AND FLIGHT PATTERNS (PUNTA ARENAS FIELD EXPERIMENT)

Date (2000)	Cloud type	Cloud top (°C)	Cloud base (°C)	Flight pattern
March 23	Ci	−50	−38	1 track ∥ wind (over sea) 2 vertical profiles
March 24	Ci	−46	−27	2 L shaped (over sea) 3 levels
March 31a	Cs	−58	?	3 tracks ∥ wind (over sea) 6 flight levels
March 31b	Ci	−62	−40	4 tracks ∥ wind (over sea) 4 flight levels
April 03	Ci (thin)	−58	−51	4 transects ⊥ wind (over sea)
	multi-layers	−45	−42	3 flight levels
April 04	Ci (thin)	−54	−45	2 transects ≈ ∥ wind (over sea)
	multi-layers	−42	−28	3 flight levels
April 05	Wave-cloud	−47	−40	4 transects ∥ wind (over mountains) 2 flight levels
April 06	Ci	−53	−34	2 transects ⊥ wind (over sea) 4 flight levels
April 10	Ci (thin)	−62	−52	4 transects ∥ wind (over sea)
	Cc	−47	−36	6 flight levels (above Lidar)
April 12	Jet-stream Ci	−51	−40	4 box patterns crossing cloud belt (over sea) 4 flight levels
April 13	Cold front Ci	−57	−52	4 transects ∥ wind and 4 levels (over sea)
	Wave-cloud	−48	−35	2 flight levels (above Lidar)

(2003) (see their Fig. 3) found small variations in the relative humidity distributions both inside and out of clouds for thresholds below ice particles concentrations of 0.1 cm^{-3}. Only cloud samples performed at temperatures lower than −25 °C are considered below. In summary, the dataset used in this study, at 1 Hz time resolution, represents 43 881 data points or about 7500 km total length of in-cloud flight.

(*c*) *Weather and synoptic situations*

In order to find air masses the least affected as possible by human impact and continental aerosols, and to measure the cirrus properties in this clean environment, the southern tip of the American continent was chosen for the INCA experiment. Punta Arenas is characterized by prevailing westerly winds and a large upstream distance to the nearest land mass, namely the Australian continent. This choice was proven correct as mainly westerly wind directions (from 250° to 310°, mean 277°) were observed in the range of altitudes considered. The synoptic situation for the measurement period in Punta Arenas from 23 March to 13 April 2000 was determined mainly by frontal systems moving frequently from the southern Pacific Ocean to the continent. It was thus possible to sample a large variety of typical midlatitude cirrus clouds associated with frontal activity. The Magallanes mountains west of Punta Arenas form an obstacle which can induce mountain waves with associated ice-cloud formation under certain atmospheric conditions.

Air masses encountered during the INCA experiment at Punta Arenas were confirmed to be rather clean with aerosol concentrations in the upper troposphere being a factor of 2–3 lower than observed in the later INCA experiment in Sep/Oct 2000 at northern midlatitudes (Minikin *et al.* 2003).

The temperature profile versus altitude inside the clouds with a mean lapse rate of -7.9 ± 1.3 K km^{-1} is close to that of the standard atmosphere (see Fig. 2). During the

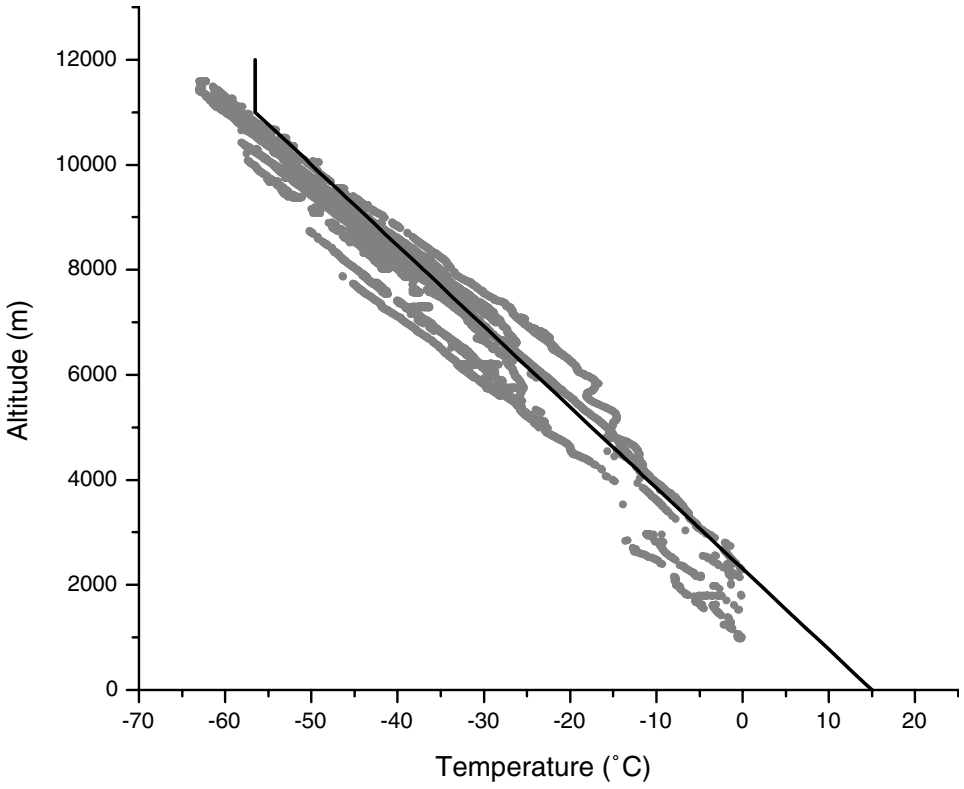

Figure 2. Scatter diagram of measured in-cloud temperature versus altitude. The solid line is the standard atmosphere for midlatitudes.

period of the INCA field observations and in the range of altitude where the clouds were sampled (between about 6000 m and 11 000 m), the mean wind speed was 44 m s^{-1}, with maximum values up to 90 m s^{-1} observed on 12 April (jet-stream cirrus case, see section 4(a)).

3. Results

Tables 2(a) and 2(b) summarize the microphysical and optical characteristics of high-altitude clouds partitioned by in-cloud flight sequences performed either at quasi-constant levels (labelled *LE* in Table 2(a)) or during climbing or descending profiles (labelled *PR* in Table 2(a)). The *LE* sequences correspond to standard deviations of the temperature of less than 1 degC (calculated over the flight sequence, see Table 2(a)). The mean values of the wind speed and direction, the air temperature and the altitude are reported with the mean relative humidity *RHi* with respect to ice. The standard deviation and the maximum value of the vertical wind component measured during the flight sequence are also shown. The cloud microphysical properties (number concentration, ice water content, extinction and effective diameter) are indicated in terms of mean, standard deviation and maximum values. The table also lists cloud optical properties, i.e. the asymmetry factor g and the halo ratio. The latter is the ratio of the radiance values measured by the Polar Nephelometer at the scattering angles of 22° and 18.5° (22° halo ratio). As discussed by Auriol *et al.* (2001), the closer the value of the ratio

to one (or more), the greater the probability of occurrence of 22° halo-related optical phenomena.

Some aerosol properties are also reported in Table 2(b) for completeness, and may serve as further comparisons. They are namely: the Aitken (*N14*), the accumulation mode (*NACC*), and the non-volatile (*NONV*) interstitial particle concentrations and the fraction of non-volatile particles within the residual particles measured by the CVI instrument. Analyses of interstitial and residual particles have been discussed in detail by Minikin *et al.* (2003) and Seifert *et al.* (2003, 2004), respectively. The variation in the aerosol values is relatively small in these sets of data. Greater differences and some correlation with ice particle properties were found by comparing data from northern and southern midlatitudes (see Fig. 7 in Seifert *et al.* 2004).

The results in Table 2(a) clearly show that most of the in-cloud data reveal significant supersaturation with respect to ice (*RHi*). Only cirrus clouds, sampled on 31 March and 10 April, are close to the equilibrium. As discussed in Ovarlez *et al.* (2002), the flight of 31 March was performed in a well-established cirrus cloud layer, with small variations of *RHi* around saturation over a large range of air temperatures. It is not clear why these two cases remain closer to the saturation equilibrium than others. Explanations were sought regarding ice water content, particle sizes, aerosol properties, vertical velocity variance, vertical temperature stratification and vertical thickness of the cloud, but no correlation was found to explain the unusual nature of these cases.

It should be mentioned that the interpretation of humidity measurements by Haag *et al.* (2003) established confidence in such measurements, showing a bias of less than 5%. In-cloud *RHi* values range from 70% to 180% with a mean value of 108%. These observations corroborate the interpretation of the observed probability distributions of *RHi* by Ovarlez *et al.* (2002) who hypothesize a relaxation time to water vapour equilibrium or a possible residual equilibrium supersaturation (Khvorostyanov and Sassen 1998). Following Haag *et al.* (2003) and Ström *et al*. (2003), these properties may be related to cirrus cloud freezing thresholds with the onset of clouds consistent with homogeneous freezing. Ice supersaturations were also observed on numerous occasions in cirrus clouds during the EMERALD-1 experiment (Gallagher *et al.* 2005), although the occurrence frequency of ice supersaturation was lower than for INCA (21% compared with 51% respectively for in-cloud data with $RHi > 105\%$). Different 'in-cloud' criteria may explain part of these differences.

A careful analysis of results in Table 2(a) reveals that for some flight sequences the mean ice particle concentration (*Conc*) reaches values significantly higher than the total mean value ($\sim$1.45 cm^{-3}, Gayet *et al.* 2004). Most flight sequences with high *Conc* values correspond to cloud types with rapid vertical transport. This feature is more pronounced for the cirrocumulus on 10 April (*Conc* $\sim$8.0 cm^{-3} during the 2130–2140 sequence), the jet-stream cirrus on 12 April (*Conc* $\sim$10.1 cm^{-3}) and the orographic-wave ice-cloud sampled during the last part of the flight on 13 April where unusually high values (*Conc* $\sim$26.7 and 47.1 cm^{-3} respectively) were found. The microphysical and optical properties of these two latter clouds will be discussed in more detail in sections 4(a) and 4(b), respectively.

High-altitude clouds with high particle concentrations have significantly smaller particle diameters (12 μm compared with 42 μm on average). This is evidenced by Fig. 3(a) which displays the maximum ice particle concentration versus the maximum updraught velocity reported during the cloud sequences. The derivation method of the vertical air speed from the Falcon aircraft measurements has been described in Bögel and Baumann (1991). An error of $\pm$10 cm s^{-1} for mean value within a flight path of 200 km (or about 20 min flight duration) is generally expected (R. Baumann,

TABLE 2(a). CIRRUS CLOUD MICROPHYSICAL AND OPTICAL PROPERTIES

Date	Segment: begin-end (h : min)	Cloud category	Sample type	Wind speed dir. (m s^{-1})	Temp.: Mean (SD) (°C)	Altitude (m) (MSL)	Vertical wind: (SD) Max (m s^{-1})	RHi (%)	Total Ice particle concentration: Mean (SD) Max (cm^{-3})	Ice particle concentration ($D > 100$ μm): Mean (SD) Max (l^{-1})
23	1507–1513		PR	10.9 270	−43.8 (2.2)	7880	(0.29) 0.55	128	1.0 (0.6) 3.3	2.2 (1.9) 9.1
March	1519–1525	Ci	LE	9.0 248	−41.9 (0.5)	7615	–	136	4.2 (2.8) 10.4	2.0 (9.3) 35.0
	1531–1539		PR	10.1 230	−38.1 (3.3)	7160	–	118	7.1 (5.3) 16.9	5.9 (11.6) 46.1
	2037–2049		LE	40.5 292	−36.8 (0.3)	7290	(0.37) 1.08	100	4.5 (2.8) 1.9	3.1 (11.0) 42.4
	2050–2107		LE	38.6 295	−37.9 (0.9)	7280	(0.30) 0.49	115	3.4 (2.5) 13.5	12.5 (8.2) 29.9
24	2107–2121		PR	31.2 298	−31.0 (3.2)	6370	(0.55) 1.34	106	2.1 (1.6) 10.8	4.6 (4.6) 28.1
March	2124–2143	Ci	LE	27.7 296	−30.0 (0.7)	6185	(0.24) 0.68	117	3.2 (2.0) 17.2	3.6 (2.9) 19.0
	2150–2214		LE	17.4 281	−28.1 (1.0)	5735	(0.22) 0.83	106	4.0 (2.6) 12.1	3.6 (2.3) 10.9
	2215–2229		LE	13.7 308	−29.0 (0.4)	5740	(0.23) 0.85	110	3.1 (2.2) 18.2	2.5 (2.1) 11.6
	2251–2258		PR	20.2 299	−28.4 (5.0)	5845	–	101	3.7 (2.2) 10.6	2.0 (0.9) 4.6
	1329–1333		PR	24.1 251	−28.5 (4.6)	6720	–	90	1.9 (1.0) 4.4	5.2 (1.4) 10.1
	1333–1342		PR	32.1 248	−44.3 (4.5)	8750	–	93	2.5 (1.2) 5.3	7.5 (2.3) 12.4
31	1354–1411		LE	40.1 267	−47.2 (0.3)	9125	(0.19) 0.49	93	1.5 (1.0) 5.8	6.6 (4.7) 19.7
March	1413–1424	Cs	LE	38.8 264	−43.2 (0.2)	8520	(0.37) 1.32	94	1.6 (1.9) 16.4	4.8 (2.8) 13.0
	1544–1550		PR	42.9 264	−49.2 (4.6)	9310	–	93	2.9 (1.4) 9.9	5.1 (2.4) 10.4
	1558–1605		PR	40.0 260	−49.8 (2.8)	9420	(0.36) 0.36	97	2.5 (1.3) 6.4	11.2 (6.4) 25.9
	1605–1611		LE	27.0 261	−39.5 (0.7)	8115	(0.28) 0.47	100	1.5 (1.1) 7.2	6.0 (4.1) 23.3
	1931–1940		PR	37.5 259	−44.5 (6.2)	9010	–	98	1.8 (0.8) 4.7	6.3 (2.0) 11.0
	1940–1948		PR	58.4 253	−57.8 (2.6)	10775	(0.05) 0.15	103	1.1 (0.6) 4.1	1.6 (1.6) 6.1
31	1955–2028		LE	68.1 263	−59.3 (0.6)	10960	(0.14) 0.49	107	1.5 (1.0) 8.3	2.2 (2.6) 11.9
March	2041–2106	Ci	LE	69.5 268	−52.0 (0.3)	10075	(0.12) 0.41	107	2.6 (1.3) 10.7	10.5 (5.2) 27.6
	2110–2154		LE	63.7 270	−45.2 (0.3)	9150	(0.13) 0.48	122	2.8 (1.1) 8.9	3.9 (3.7) 23.1
	2158–2220		LE	60.0 278	−39.6 (0.2)	8240	(0.21) 1.58	102	1.5 (0.7) 4.4	5.7 (4.2) 20.2
	2238–2251		PR	47.3 254	−44.2 (6.6)	9105	(0.27) 0.60	93	0.7 (0.4) 3.2	5.4 (2.3) 13.2
	1925–1931		PR	19.6 298	−36.3 (5.5)	7550	–	–	3.9 (4.4) 20.7	12.3 (10.3) 38.8
	1950–1959	Ci(thin)	LE	25.1 290	−49.1 (0.1)	9075	(0.13) 0.36	85	0.3 (0.2) 0.7	2.9 (1.4) 7.7
03	2011–2022	multi-	LE	28.5 285	−54.4 (0.3)	9670	(0.17) 0.48	126	0.6 (0.8) 4.4	1.7 (1.6) 7.9
April	2051–2125	Layers	LE	33.0 290	−52.4 (0.9)	9420	(0.16) 0.51	104	0.8 (1.0) 5.1	2.5 (4.7) 20.4
	2137–2150		PR	32.0 285	−45.8 (4.0)	8640	(0.27) 0.73	115	1.8 (1.6) 8.8	7.5 (6.5) 29.4
	2207–2217		PR	29.3 286	−52.3 (2.1)	9475	(0.28) 0.39	120	0.9 (0.5) 2.4	6.0 (4.9) 17.6
	1856–1916		LE	36.8 250	−52.6 (0.2)	9740	(0.11) 0.31	113	0.7 (0.4) 2.2	3.0 (1.9) 10.1
04	1924–1944	Ci(thin)	LE	40.5 264	−47.3 (0.9)	9185	(0.25) 0.52	109	0.7 (0.4) 2.4	2.8 (2.3) 12.6
April	1951–1959	multi-	PR	37.9 273	−41.2 (4.2)	8470	–	105	1.0 (0.7) 3.8	4.2 (2.8) 12.5
	2000–2015	Layers	PR	33.6 272	−31.9 (3.3)	7410	(0.12) 0.37	106	2.0 (1.7) 14.1	2.5 (2.6) 20.8
	2015–2032		LE	32.6 259	−41.2 (1.0)	8465	(0.13) 0.58	104	1.5 (1.0) 5.4	3.4 (3.3) 24.8
5	1711–1725	Wave-	PR	21.8 288	−43.5 (3.7)	9290	(0.13) 0.62	108	4.4 (5.3) 23.0	10.1 (10.5) 45.5
April	1737–1825	cloud	LE	19.4 275	−46.6 (0.2)	9530	(0.45) 1.54	108	3.8 (4.3) 34.7	8.9 (8.6) 48.8
	1911–1952		LE	17.6 279	−43.7 (0.2)	9220	(0.56) 2.31	103	5.9 (5.9) 32.1	10.5 (7.9) 39.8
	1839–1847		PR	47.6 312	−41.0 (2.4)	8130	(0.18) 0.29	104	1.3 (0.6) 3.9	5.7 (3.9) 21.1
06	1851–1910		LE	55.7 313	−37.8 (0.2)	7560	(0.16) 0.60	109	1.5 (1.1) 5.4	0.9 (1.0) 5.2
April	1925–2009	Ci	LE	60.7 310	−44.8 (1.0)	8480	(0.18) 0.71	114	1.6 (1.5) 8.5	4.4 (6.4) 42.7
	2024–2100		LE	53.3 310	−42.0 (1.0)	8130	(0.14) 0.61	110	2.0 (1.8) 9.4	6.6 (8.7) 47.0
	2125–2136		PR	35.8 317	−34.3 (3.8)	7515	(0.20) 0.45	114	3.0 (2.4) 11.4	4.7 (4.4) 19.2
	1947–1954	Ci(thin)	PR	23.9 252	−42.3 (3.2)	8780	–	100	0.5 (0.8) 4.9	2.1 (2.4) 12.0
10	2008–2125		LE	38.6 240	−59.4 (0.9)	11170	(0.22) 0.55	97	0.6 (0.9) 6.7	0.0 (0.0) 0.3
April	2130–2140	Cc	PR	25.2 260	−37.7 (2.3)	8115	(0.31) 0.66	99	8.0 (6.6) 29.6	13.0 (11.5) 53.6
	2204–2237		LE	49.3 255	−53.6 (0.9)	10530	(0.12) 0.37	94	0.7 (0.4) 2.5	3.4 (2.2) 10.5
	2254–2304		PR	36.5 242	−52.4 (4.1)	10225	–	95	4.4 (7.1) 38.9	2.7 (3.0) 13.8
	1302–1309		PR	76.3 291	−29.8 (3.6)	7000	–	–	4.4 (2.9) 13.6	13.7 (9.2) 36.3
	1313–1340	Jet-	LE	89.8 293	−48.4 (1.0)	9525	(0.56) 1.47	123	2.4 (3.2) 15.9	4.3 (4.2) 21.9
12	1356–1408	stream	LE	82.9 298	−51.0 (0.1)	9815	(0.48) 1.56	146	10.1 (8.2) 40.3	15.8 (11.5) 42.9
April	1424–1500	Ci	LE	84.1 299	−46.8 (1.1)	9325	(0.40) 1.35	124	6.4 (5.9) 25.8	12.4 (10.3) 36.8
	1515–1529		LE	81.1 299	−40.1 (0.1)	8580	(0.27) 1.00	162	5.3 (5.0) 33.0	13.3 (8.8) 38.1
	1547–1556		PR	87.1 295	−43.7 (2.9)	8960	(0.56) 1.00	22	3.5 (4.2) 15.9	12.0 (12.8) 51.5
	1720–1732	Cold-	PR	39.7 276	−36.9 (9.5)	7890	(0.07) 0.14	112	7.7 (15.7) 90.4	5.0 (6.7) 40.9
13	1739–1750	Front Ci	LE	38.4 273	−34.8 (0.1)	7565	(0.36) 0.57	105	3.8 (2.4) 11.1	13.6 (11.3) 49.8
April	1753–1818		LE	38.3 272	−40.1 (1.0)	8345	(0.33) 0.58	101	3.1 (2.6) 14.6	13.3 (9.3) 41.4
	1934–2002	Wave-	LE	36.2 267	−47.3 (0.7)	9375	–	106	26.5 (9.5) 61.9	1.2 (3.5) 27.2
	2011–2034	cloud	LE	35.3 278	−41.9 (2.9)	8695	–	114	47.1 (26.9) 116.0	0.2 (0.4) 3.3

The cirrus cloud microphysical and optical properties are partitioned by flight sequences performed either at constant levels or profiles obtained during climb or descent (labelled *LE* and *PR* respectively). Mean values of the wind speed and direction, air temperature, altitude, and relative humidity with respect to ice (RHi), standard deviations and the maximum values of the vertical wind component measured during the flight sequence are given. The cloud microphysical properties (number concentration, ice water content, extinction coefficient, and effective diameter) are indicated in terms of mean, standard deviation and maximum values. Also listed are cloud optical properties, i.e. asymmetry factor and halo ratio. The aerosol properties are characterized by the number density of Aitken (N14; condensation particles larger than 14 nm), of the accumulation mode (NACC; from PCASP-100X in the size range 0.12–1 μm), and of the non-volatile (NONV; total condensation particles downstream of the 250 °C thermodenuder) interstitial particles. Moreover, the fraction of non-volatile residual particles is listed as measured by the CVI instrument.

TABLE 2(b). CIRRUS CLOUD MICROPHYSICAL AND OPTICAL PROPERTIES (CONTINUED)

Date	Segment: begin-end (h : min)	Ice water content: Mean (SD) Max (mg m^{-3})	Extinction coefficient Mean (SD) Max (km^{-1})	Effective diameter Mean (SD) Max (μm)	Asymmetry parameter Mean (SD)	Halo ratio	Aerosol N14 (cm^{-3})	Aerosol NACC (cm^{-3})	Aerosol NONV (cm^{-3})	Aerosol CVI (cm^{-3})
23	1507–1513	4.6 (2.5) 11.5	0.32 (0.20) 0.92	55.8 (31.4) 185.6	0.770 (0.005)	–	180.8	4.1	6.6	–
March	1519–1525	16.3 (9.3) 34.5	1.25 (0.73) 3.01	43.1 (18.8) 111.9	0.774 (0.005)	0.70	323.6	2.1	6.0	85.2
	1531–1539	27.8 (17.6) 68.6	2.17 (1.48) 4.61	46.9 (24.7) 154.9	0.770 (0.009)	0.73	125.8	3.8	3.7	50.0
	2037–2049	17.7 (11.6) 46.9	1.55 (0.94) 3.97	33.5 (11.5) 73.7	0.763 (0.012)	0.65	259.3	7.8	10.8	–
	2050–2107	18.1 (9.3) 48.5	1.17 (0.80) 4.04	54.3 (22.6) 165.3	0.770 (0.006)	0.71	353.5	14.5	6.2	10.0
24	2107–2121	19.0 (14.0) 70.6	0.64 (0.44) 2.26	91.5 (34.5) 210.8	0.771 (0.010)	0.68	474.1	23.5	9.8	26.0
March	2124–2143	25.5 (15.6) 82.0	0.84 (0.45) 2.52	92.9 (29.9) 207.3	0.776 (0.008)	0.70	651.1	29.7	8.4	32.9
	2150–2214	31.3 (22.0)122.4	1.04 (0.66) 3.05	88.1 (25.9) 183.3	0.768 (0.005)	0.72	532.5	23.4	12.9	30.5
	2215–2229	17.5 (12.2) 76.1	0.71 (0.44) 2.57	77.5 (29.5) 214.1	0.767 (0.005)	0.74	440.2	14.9	10.8	26.8
	2251–2258	14.2 (9.6) 60.9	0.76 (0.46) 2.28	56.7 (19.8) 171.2	0.770 (0.006)	0.69	592.3	33.2	14.2	28.3
	1329–1333	18.8 (10.2) 46.1	0.62 (0.25) 1.23	86.8 (15.4) 119.1	0.761 (0.002)	0.68	531.6	4.1	2.7	41.0
	1333–1342	12.1 (3.3) 19.3	1.03 (0.40) 1.85	38.4 (10.0) 70.3	0.766 (0.003)	0.65	197.6	2.8	4.1	38.4
31	1354–1411	8.6 (5.7) 26.9	0.63 (0.36) 1.95	42.0 (15.4) 98.3	0.771 (0.008)	0.62	118.0	4.6	4.2	32.7
March	1413–1424	7.2 (4.8) 27.2	0.54 (0.40) 3.28	41.7 (12.3) 82.5	0.762 (0.011)	0.57	192.3	2.1	1.9	27.9
	1544–1550	9.9 (3.2) 19.7	0.92 (0.26) 2.20	33.2 (8.8) 59.1	0.765 (0.004)	0.69	58.5	2.6	3.8	35.0
	1558–1605	13.8 (6.8) 30.0	0.98 (0.49) 2.17	42.7 (10.8) 77.2	0.775 (0.009)	0.73	65.5	4.9	3.8	34.6
	1605–1611	12.4 (5.1) 36.8	0.56 (0.38) 2.21	75.3 (21.7) 131.2	0.772 (0.006)	0.69	265.6	7.7	2.0	28.8
	1931–1940	10.0 (3.4) 18.7	0.60 (0.26) 1.61	54.6 (14.9) 105.9	0.769 (0.003)	0.68	130.9	2.9	5.7	37.1
	1940–1948	3.3 (2.0) 9.6	0.36 (0.20) 1.08	26.1 (7.9) 45.2	0.761 (0.009)	0.68	89.0	3.5	9.1	41.7
31	1955–2028	4.8 (3.4) 17.3	0.50 (0.31) 1.74	28.9 (17.6) 143.8	0.765 (0.010)	0.74	49.6	3.7	4.8	39.4
March	2041–2106	16.8 (7.7) 46.3	0.99 (0.47) 3.59	56.5 (22.7) 131.3	0.784 (0.005)	0.77	60.2	5.2	3.3	38.3
	2110–2154	15.4 (7.8) 45.3	0.68 (0.32) 2.19	68.8 (21.5) 176.6	0.774 (0.004)	0.79	108.4	21.1	3.4	38.6
	2158–2220	12.9 (6.6) 37.6	0.53 (0.24) 1.45	74.4 (27.2) 207.8	0.773 (0.009)	0.78	96.2	6.0	3.3	29.8
	2238–2251	5.0 (1.9) 14.3	0.32 (0.18) 1.42	54.0 (14.7) 106.8	0.762 (0.006)	0.71	52.4	2.7	3.4	30.0
	1925–1931	20.0 (19.2) 94.0	1.17 (1.12) 5.17	52.8 (20.9) 114.6	0.756 (0.015)	0.65	181.1	4.7	11.1	47.2
	1950–1959	3.0 (1.2) 5.7	0.14 (0.06) 0.30	64.8 (18.3) 101.5	0.753 (0.009)	0.70	102.7	5.4	9.5	40.5
03	2011–2022	2.4 (2.0) 9.6	0.15 (0.13) 0.81	53.7 (34.6) 126.4	0.758 (0.010)	0.62	86.9	6.5	8.8	40.7
April	2051–2125	3.6 (6.0) 29.2	0.30 (0.45) 2.41	31.2 (13.5) 90.3	0.756 (0.013)	0.70	77.1	3.2	8.3	33.3
	2137–2150	10.0 (8.5) 37.8	0.73 (0.70) 3.86	46.9 (18.0) 115.5	0.765 (0.009)	0.77	97.7	10.9	9.9	41.3
	2207–2217	9.8 (5.7) 26.4	0.35 (0.24) 1.22	95.8 (38.0) 203.9	0.784 (0.009)	0.61	89.5	7.4	8.2	45.1
	1856–1916	5.4 (2.9) 12.2	0.25 (0.18) 0.93	79.8 (30.6) 187.2	0.772 (0.006)	0.63	66.0	9.8	10.2	39.4
04	1924–1944	5.0 (3.9) 24.6	0.21 (0.14) 0.67	77.3 (35.8) 205.1	0.770 (0.006)	0.65	94.8	8.0	4.7	40.0
April	1951–1959	8.4 (6.5) 32.6	0.34 (0.21) 0.96	73.4 (29.9) 153.8	0.770 (0.007)	0.65	128.2	9.6	6.5	34.4
	2000–2015	12.7 (12.5) 68.4	0.44 (0.37) 2.65	79.7 (35.9) 162.0	0.768 (0.005)	0.71	67.0	2.1	2.5	38.3
	2015–2032	12.3 (8.8) 35.5	0.39 (0.29) 1.82	94.3 (36.1) 234.4	0.773 (0.006)	0.79	88.3	2.4	2.1	34.6
05	1711–1725	21.1 (20.1) 79.0	1.12 (1.20) 5.30	63.2 (30.3) 169.7	0.770 (0.004)	0.71	237.7	2.7	3.8	51.9
April	1737–1825	15.5 (16.6) 118.6	1.10 (1.01) 6.46	39.8 (13.2) 121.4	0.766 (0.006)	0.68	63.4	3.1	4.6	51.9
	1911–1952	18.8 (14.7) 77.3	1.48 (1.16) 6.01	39.0 (11.3) 87.7	0.761 (0.004)	0.75	91.1	7.6	3.8	47.6
	1839–1847	8.3 (3.8) 23.2	0.45 (0.28) 1.27	64.5 (24.8) 148.5	0.767 (0.004)	0.44	111.2	4.2	3.2	40.5
06	1851–1910	7.5 (10.4) 78.5	0.28 (0.23) 1.00	62.6 (42.4) 194.9	0.777 (0.006)	0.60	116.7	4.0	1.8	39.5
April	1925–2009	14.7 (13.6) 87.6	0.44 (0.45) 3.39	108.5 (37.3) 265.3	0.780 (0.007)	0.74	89.2	4.5	4.2	39.5
	2024–2100	15.2 (12.5) 67.8	0.62 (0.71) 3.90	90.6 (38.5) 253.8	0.774 (0.007)	0.75	97.2	4.0	2.1	38.5
	2125–2136	16.3 (13.9) 76.2	0.63 (0.45) 2.29	74.6 (35.3) 222.0	0.775 (0.008)	0.73	147.0	8.5	8.5	42.6
	1947–1954	4.1 (6.3) 38.2	0.15 (0.20) 0.86	74.9 (35.2) 184.4	0.743 (0.022)	0.61	120.6	5.5	11.4	–
10	2008–2125	0.4 (0.4) 2.0	0.07 (0.07) 0.49	16.8 (6.7) 33.5	0.749 (0.017)	0.69	65.1	7.0	12.7	–
April	2130–2140	18.5 (10.1) 50.0	1.68 (1.04) 4.62	44.1 (27.6) 126.8	0.767 (0.006)	0.73	148.4	10.7	12.1	42.4
	2204–2237	4.8 (2.5) 11.8	0.40 (0.23) 1.19	39.4 (9.9) 88.4	0.762 (0.014)	0.72	65.3	3.4	10.6	40.7
	2254–2304	6.5 (6.7) 28.1	0.81 (0.93) 4.23	26.8 (9.1) 69.1	0.763 (0.014)	0.70	75.8	6.8	10.9	37.5
	1302–1309	32.5 (20.5) 81.5	1.31 (0.72) 3.45	75.3 (32.3) 172.5	0.758 (0.011)	0.62	127.8	5.1	18.9	66.4
	1313–1340	8.5 (9.8) 69.9	0.72 (0.79) 3.73	34.8 (12.4) 93.0	0.754 (0.016)	0.60	49.8	10.3	7.0	43.7
12	1356-1408	30.9 (22.3) 78.5	2.51 (1.70) 6.96	35.3 (9.4) 84.1	0.766 (0.007)	0.70	49.8	6.0	8.7	39.2
April	1424–1500	23.3 (21.7) 108.0	1.79 (1.40) 5.84	36.7 (9.1) 75.7	0.764 (0.008)	0.70	68.9	5.7	11.2	–
	1515–1529	28.6 (23.3) 131.0	1.39 (1.00) 5.79	61.2 (21.1) 152.0	0.760 (0.005)	0.73	73.5	12.4	8.6	45.7
	1547–1556	12.0 (12.8) 51.5	0.83 (0.90) 3.72	44.8 (12.9) 90.0	0.751 (0.016)	0.62	54.8	10.3	5.8	41.9
	1720–1732	14.0 (14.6) 69.3	1.10 (1.35) 7.24	57.8 (32.1) 134.7	0.772 (0.016)	0.59	78.3	7.6	8.3	50.0
13	1739–1750	34.7 (17.6) 74.2	1.11 (0.68) 3.36	100.5(29.0)187.9	0.769 (0.006)	0.73	60.8	7.7	7.6	45.5
April	1753–1818	20.5 (13.8) 72.4	1.00 (0.78) 4.18	70.1 (26.9) 141.7	0.767 (0.007)	0.81	130.7	8.7	10.8	–
	1934–2002	14.3 (9.5) 57.4	3.15 (1.25) 7.52	12.8 (3.5) 29.4	0.772 (0.005)	0.73	72.2	2.3	12.3	–
	2011–2034	21.2 (10.9) 48.5	5.34 (2.89) 12.65	12.1 (2.7) 26.0	0.767 (0.012)	0.72	53.3	2.1	7.3	40.0

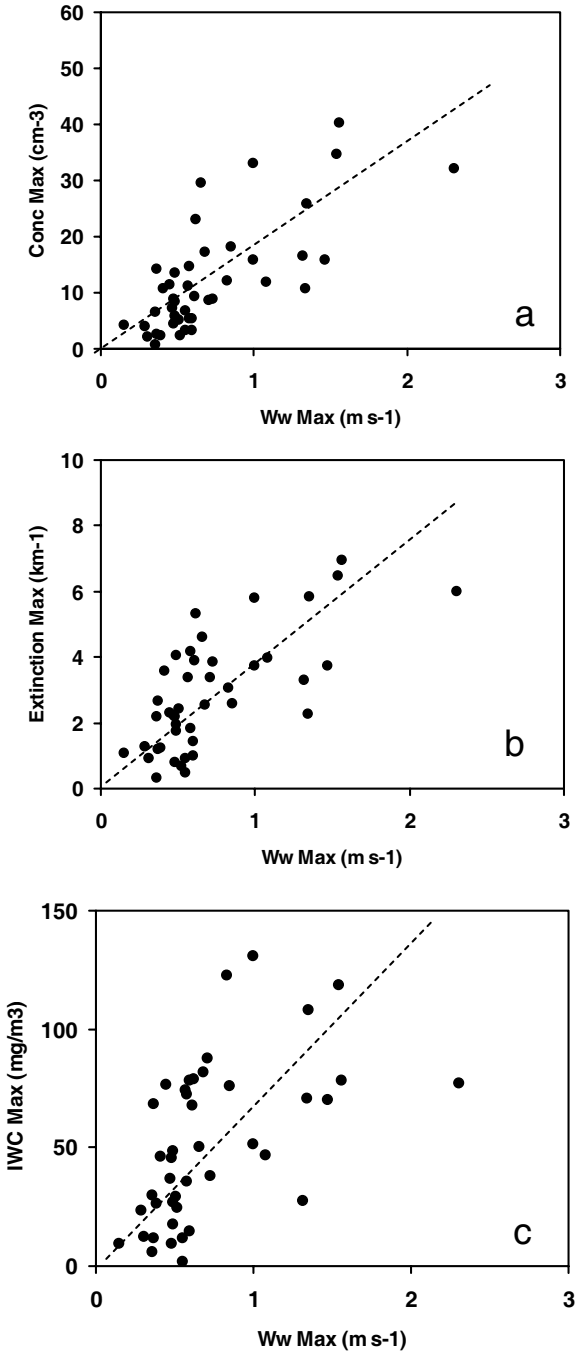

Figure 3. Maximum values of microphysical parameters versus the maximum values of the updraught velocity observed during the cloud sequences: (a) ice particle concentration, (b) extinction coefficient and (c) ice water content. The dashed lines indicate the mean value relationships.

private communication). In most of the *PR* flight sequences (see Table 2(a)), the vertical wind component was not calculated since the required stabilized flight paths were lacking in necessary length. The dispersion of the data points seen in Fig. 3(a) may be partially explained by the fact that the maximum ice concentration and the maximum updraught velocity (and subsequently the in-cloud supersaturation) do not necessarily occur at the same location and time. Nevertheless, the results show that high ice particle concentrations are typically found in places where the vertical velocity is high. The dynamics of particle formation may cause additional dispersion of the data points. Similar relationships are found on Figs. 3(b) and 3(c) which display the maximum values of the extinction coefficient and the ice water content versus the updraught velocity respectively.

Figure 3(a) corroborates the cloud-free parametrization of Kärcher and Lohmann (2002), who predict that the number density of ice crystals in cirrus increases more than linearly with the updraught velocity. For 1 m s^{-1} vertical velocity and temperatures between $-33\,^{\circ}$C and $-53\,^{\circ}$C, they predict a cirrus crystal number density of about 20 to 100 cm^{-3}. The fact that actual observations show 2–3 times fewer crystals than the above theoretical predictions may be in part due to the presence of presumably few but large pre-existing crystals. Indeed, subsequent vapour depletion may prevent further nucleation of new ice crystals if the uplift is insufficient (Kärcher *et al*. 2006).

The probability of finding supercooled liquid water droplets in mixed-phase clouds diminishes with decreasing temperature. Observations indicating the presence of liquid droplets have been reported in the literature for temperatures down to approximately $-40\,^{\circ}$C (Heymsfield 1993). As previously discussed, the Polar Nephelometer measurements are reliable for extinction values down to 0.02 km^{-1}, i.e. for particle concentration down to about 0.1 cm^{-3}. Therefore, liquid water occurrence can be accurately evidenced among ice particle population according to significant contrasts of the asymmetry parameter values between water (spherical) droplets ($g > 0.8$) and ice particles ($g < 0.8$). During the experiment in Punta Arenas, supercooled water droplets and subsequent mixed-phase conditions were rarely observed and the corresponding in-cloud sequences lasted only a few dozen seconds. This may be explained by the flight patterns which were mainly oriented to cirrus observations. The lowest temperature at which some supercooled water droplets were detected was $-33\,^{\circ}$C. This feature was related to altostratus clouds with rapid updraught sampled during flights on 4 April and 13 April (see the case-study discussed in section 4(b)).

A quantitative overview of the microphysical and optical properties of midlatitude cirrus in the southern hemisphere is presented versus air temperature in Fig. 4. In order to preserve the homogeneity of the observations for comparison with previous (or future) cirrus climatologies, the jet-stream cirrus and the orographic-wave iced-cloud observations have been removed from the dataset. They represent about 10% of all observations collected during the INCA southern hemisphere experiment. Figure 4 displays the median values and the quartiles of distributions binned into 5 degC intervals of the air temperature (from $-25\,^{\circ}$C to $-60\,^{\circ}$C), of the ice particle concentration (*Conc*), the concentration of particles with diameter larger than 100 μm (*C100*), the ice water content (*IWC*), the extinction coefficient (*Ext*), the effective diameter (*Deff*), and the asymmetry parameter (g), respectively. The microphysical properties of midlatitude cirrus clouds observed in the southern hemisphere during INCA are of the same order of magnitude as found in previous works (mainly in the northern hemisphere) in terms both of median values and quartiles. In particular, they are similar to those collected for a variety of cirrus types, locations and time of year and reported in Heymsfield and McFarquhar (2002), as displayed in Figs. 4(b), 4(c) and 4(d), where the ranges of variation of the median

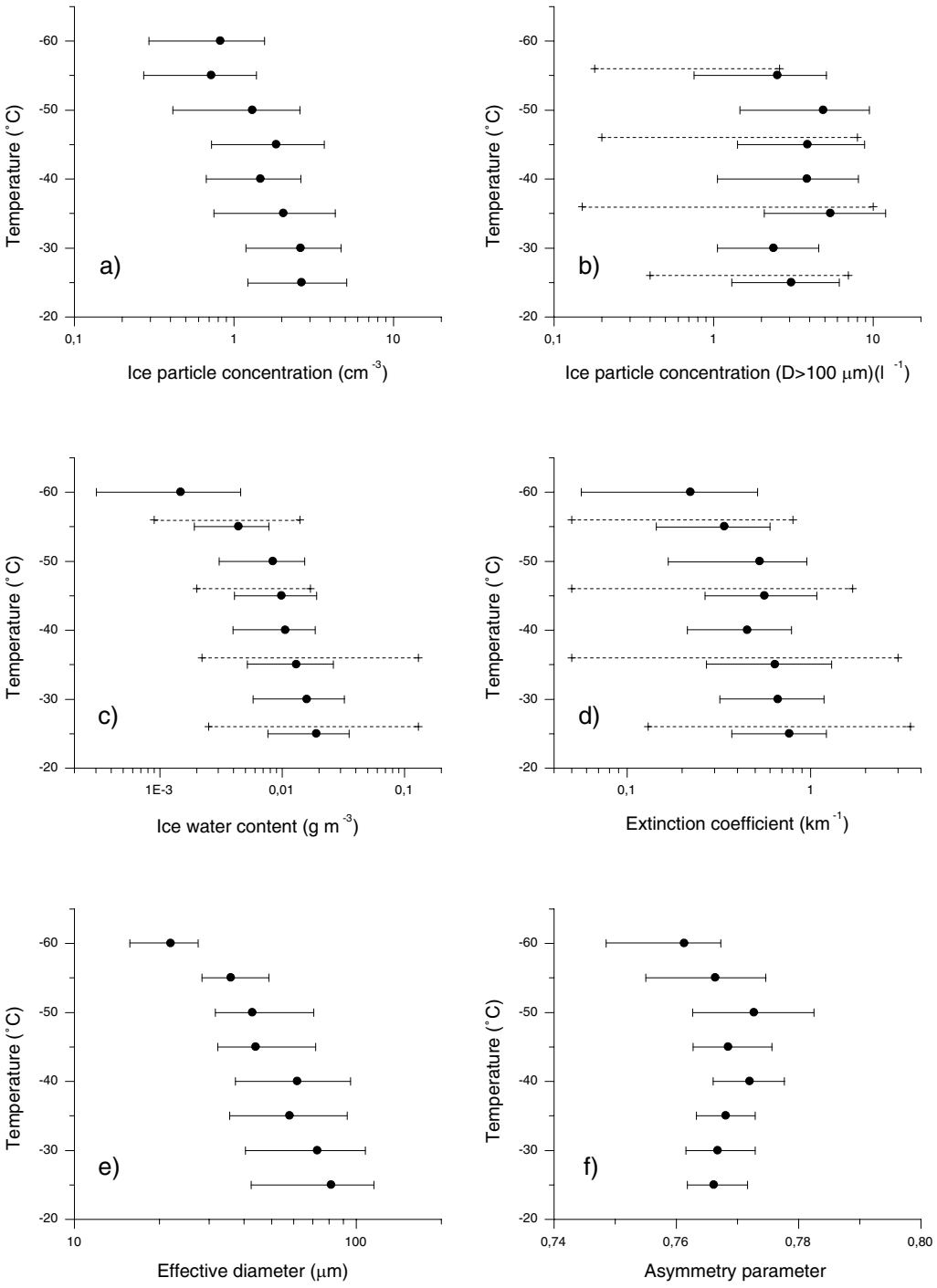

Figure 4. Microphysical and optical cirrus cloud parameters versus the air temperature. Filled circles represent median values and horizontal bars span the 25% and 75% quartiles of the distributions: (a) ice particle concentration, (b) concentration of ice particles with $D > 100$ μm, (c) ice water content, (d) extinction coefficient, (e) effective diameter and (f) asymmetry parameter. Dotted lines in (b), (c) and (d) represent the ranges of variation of median values reported by Heymsfield and McFarquhar (2002).

values have been superimposed over our results. Our results have also been compared to recent observations made by Lawson *et al.* (2006b). For temperatures below −40 °C, the values of microphysical parameters are similar but larger *IWC* and extinction values are found by these authors at warmer temperatures.

It should be pointed out that most of the results referenced by Heymsfield and McFarquhar (2002) do not consider the contribution of small ice crystals (i.e. $D \lesssim 20$ μm). According to our investigations, the small ice crystals (measured by the FSSP-300) represent about 8% of the *IWC*, but contribute about 35% to the total extinction. The results in Fig. 4(a) show that the mean ice particle concentration decreases with decreasing temperature, from 2.2 cm^{-3} near −25 °C to 0.5 cm^{-3} at −60 °C. Concerning the concentration of particles having a diameter larger than 100 μm (ranging from 2 l^{-1} to 5 l^{-1}), no apparent relationship can be found as regards temperature but far smaller values (0.3 l^{-1}) are observed at the lowest temperatures (Fig. 4(b)). As expected, the ice water content and the extinction coefficient decrease with decreasing temperature from about 18 mg m^{-3} to 0.05 mg m^{-3} (Fig. 4(c)) and from 0.7 km^{-1} to 0.08 km^{-1} (Fig. 4(d)), respectively. A similar trend is observed for the effective diameter which decreases from about 80 μm to 17 μm (Fig. 4(e)). This feature is consistent with previous observations in cirrus by Francis *et al.* (1998) and by Boudala *et al.* (2002) although their effective radius absolute values differed since different methods were used to derive the ice particle size.

The dependence of the microphysical properties on temperature reflects the variation of the saturation vapour density with temperature. At low temperatures less water vapour is available for the growth of ice crystals; therefore the ice water content values are lower than those noted at higher temperatures (Heymsfield and Donner 1990). Moreover, sedimentation of ice crystals tends to deplete the largest ice crystals at high levels with low temperatures, and transports them towards lower levels with higher temperatures.

Figure 4(f) shows that the asymmetry parameter g mainly increases from 0.766 at −25 °C to 0.772 at −50 °C, then decreases to 0.758 at −60 °C. As reported by Gayet *et al.* (2004), these rather small variations with temperature with a narrow scatter (80% of g values are within the range 0.76 to 0.78) highlight the fairly uniform optical properties of the cirrus clouds sampled.

4. Two illustrative case-studies

In this section we describe two case-studies that illustrate in greater detail certain characteristics of the 'particular' high-level clouds summarized in the previous section. Although these cases are not representative of the majority of cirrus measurements during the INCA experiment, they have been selected because they show cloud formation in air masses with rapid upward motions and with similar aerosol properties but very different cloud particle and humidity properties. The presentation of these two case-studies is also motivated by the fact that only a few *in situ* observations have been reported on jet-stream cirrus. More detailed observations (and subsequent interpretation on cloud formation) come from remote sensing measurements (see for instance Sassen *et al.* 1995 and Haynes and Stephen 2002). Wave-clouds which are characterized by relatively simple and quasi-steady-state dynamical and microphysical frameworks can be used as natural laboratories to gain an understanding of ice nucleation processes at temperatures below −30 °C (see, among others, Heymsfield and Miloshevish 1993; Field *et al.* 2001; Baker and Lawson 2006).

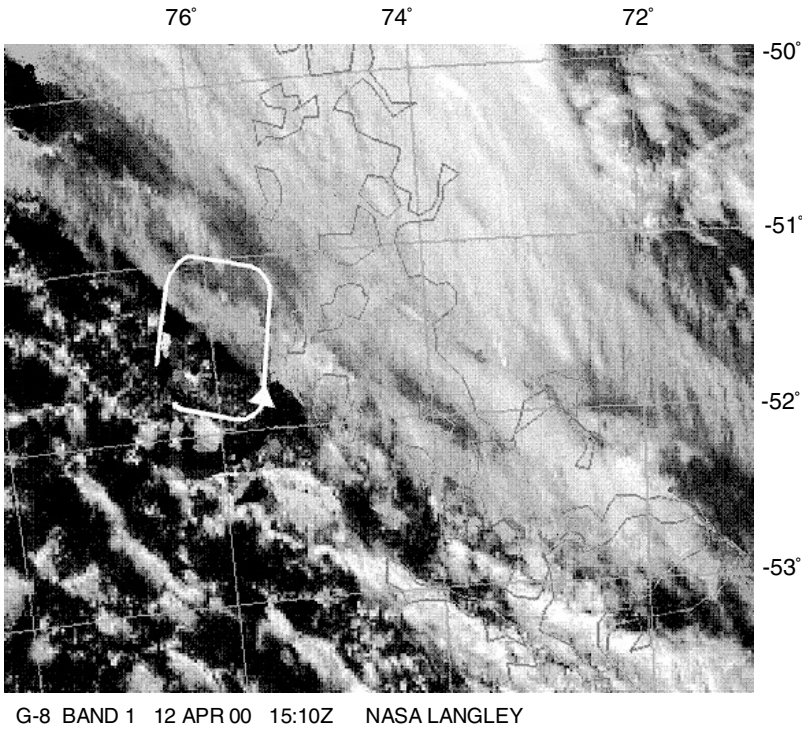

Figure 5. Satellite picture for 1510 UTC 12 April 2000 from GOES in the visible channel. The Falcon flight trajectory is superimposed to the satellite picture.

(*a*) *Jet-stream cirrus (flight on 12 April)*

On 12 April, a strong jet stream was found in front of a trough moving to the southern tip of South America. The backward trajectories calculated from ECMWF analyses for the times and positions of the measurement flight show that the air mass had moved within the previous five days from the southern Atlantic and the Indian Ocean eastwards to the experimental area with no general change in altitude, and without leaving the storm belt between 50° and 70° South. The greatest distances were found for destination levels in the upper part of the jet region between 200 and 250 hPa. Here the 5-day back-trajectories start from 20°W and 60°S. Only at levels below 750 hPa were the origins of the trajectories found to be over the Pacific. The circulation associated with the jet stream forced cirrus development on the updraught side, while the subsidence in the poleward part of the jet resulted in the very dry conditions of a stratospheric intrusion, which was also indicated by enhanced ozone concentrations. The sharp boundary (see Fig. 5) made it possible to probe this quasi-stationary dynamical system at four different levels within two hours, passing the tropopause on horizontal flight legs. The edge of the cloud field connected to the jet stream is clearly visible in the satellite picture, see Fig. 5 (GOES visible channel at 1510 UTC). A flight box pattern was planned with one leg each in the clouds then in the cloud-free air, respectively, and two intermittent legs directed towards the humidity gradient, i.e. perpendicular to the wind (see the superimposed flight trajectory on Fig. 5). This box was flown at four different levels.

Figures 6(a) to 6(f) represent the vertical profiles of several microphysical and optical parameters obtained during the flight of the Falcon aircraft in the jet-stream cirrus between 1320 and 1600 UTC. Despite the large fluctuations of the considered parameters, mainly due to the natural cloud inhomogeneities, the largest concentration of ice particles ($\sim$40 cm^{-3}, Fig. 6(a)) and the smallest effective diameter ($\sim$40 μm, Fig. 6(e)) as well as the smallest ice water content ($\sim$0.04 g m^{-3}, Fig. 6(b)) are observed at the cloud top (9800 m/$-$51 °C). Rather high ice water content and extinction coefficient values (0.14 g m^{-3} and 11 km^{-1} respectively, Fig. 6(c)) are evidenced at the lowest flight level (8600 m/$-$40 °C). The asymmetry parameter (Fig. 6(f)) increases slightly with altitude (with a mean value around 0.760).

In order to discuss the cloud horizontal structure along the flight track depicted in Fig. 5, Fig. 7 presents a time series of the cloud parameters together with the vertical wind component (*Ww*) and the relative humidity (*RHi)* with respect to the ice. These parameters were obtained during a 17-minute in-cloud flight sampling at the lowest observed level ($\sim$8600 m/$-$40 °C). The location of the cirrus with properties displayed in Fig. 7 can be closely related to the cloud belt geometry seen in Fig. 5 as the corresponding time sequence of the flight is within $\sim$15 min of the satellite overpass time. At 15:14:40 the Falcon penetrated the sharp poleward edge of the cirrus following the flight trajectory shown in Fig. 5, and then traversed the cloud belt to reach clear air before turning back into the cloud belt at $\sim$1521 UTC. Indeed, rather symmetrical cloud properties are observed in Fig. 7 since the aircraft came out of the same cirrus poleward edge seven minutes later. Very strong moisture gradients are evidenced near the cloud poleward boundaries, where the relative humidity in clear air is only about 30% (at any sampled level) and where significant downdraughts (down to $-$0.5 m s^{-1}) are measured. The subsidence in the poleward part of the jet stream resulted in the very dry conditions of a stratospheric intrusion. For approximately 80 s (i.e. $\sim$14 km) from the cloud poleward edges, the microphysical properties are characterized by rather large ice crystals (*Deff* between 80 μm and 140 μm). Figure 8(a) illustrates an example of results observed in these areas (sampled between 15:15:00 and 15:15:30, see Fig. 7). The upper panel displays the PMS FSSP-300 and 2D-C particle size distributions (with the values of the parameters), whereas the lower panel represents the measured (Polar Nephelometer) scattering phase function with some examples of 2D-C ice crystal images. The results show bullet–rosette shapes with a bimodal size distribution and an asymmetry factor of 0.768. The corresponding ice particle concentration, ice water content and extinction are 3.8 cm^{-3}, 26 mg m^{-3} and 0.9 km^{-1} respectively. In these cloud regions the ice particles still grow, due to significant supersaturated relative humidity (131%).

In the middle section of the cloud belt (around 15:17:30 and 15:25:30 in Fig. 7, respectively), rapid updraughts (up to 0.7 m s^{-1}) are observed with very high ice supersaturation. We note in passing that because of the very strong moisture gradients in these areas, the time response of the humidity probe (i.e. 7 s, Ovarlez *et al.* 2000) may significantly hamper the accuracy of the absolute high *RHi* values (which were therefore truncated in Fig. 6 for *RHi* $>$ 150%, i.e. the value of the expected homogeneous nucleation at $-$40 °C, Koop *et al.* 2000). Figure 8(b), with a similar representation as in Fig. 8(a), displays the results observed in the 'peak' region between 15:25:30 and 15:25:36 (see Fig. 7) where large values of the ice particle concentration, ice-water content and extinction are highlighted (29 cm^{-3}, 109 mg m^{-3} and 5 km^{-1}, respectively). 2D-C ice crystal images reveal irregular shapes and some bullet–rosettes with a bimodal size distribution and an asymmetry factor of 0.761. From these results it may be concluded that the middle section of the cloud belt constitutes the ice-generating

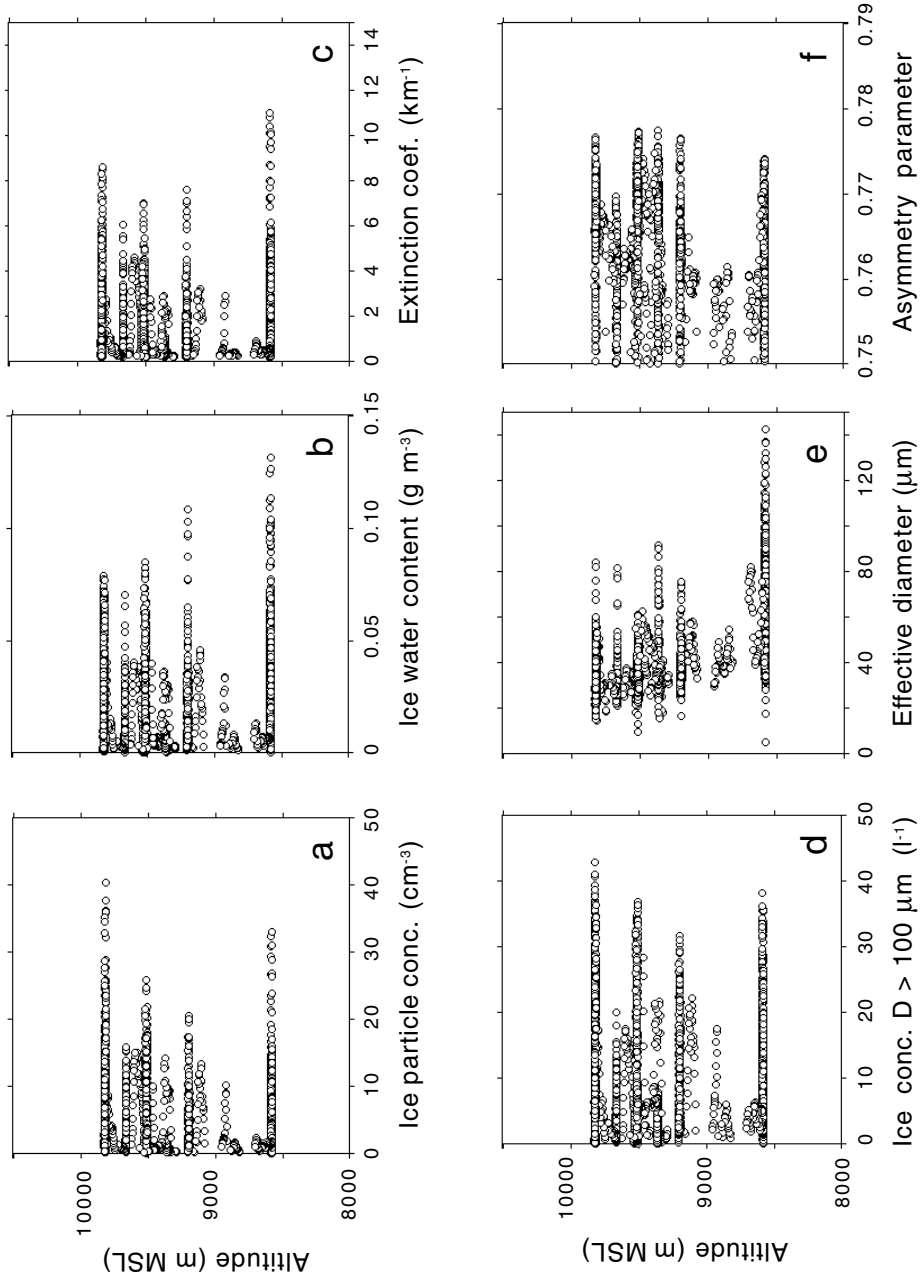

Figure 6. Microphysical and optical cloud parameters versus the altitude obtained in jet-stream cirrus cloud on 12 April: (a) ice particle concentration, (b) ice water content, (c) extinction coefficient, (d) concentration of ice particles with $D > 100$ μm, (e) effective diameter and (f) asymmetry parameter.

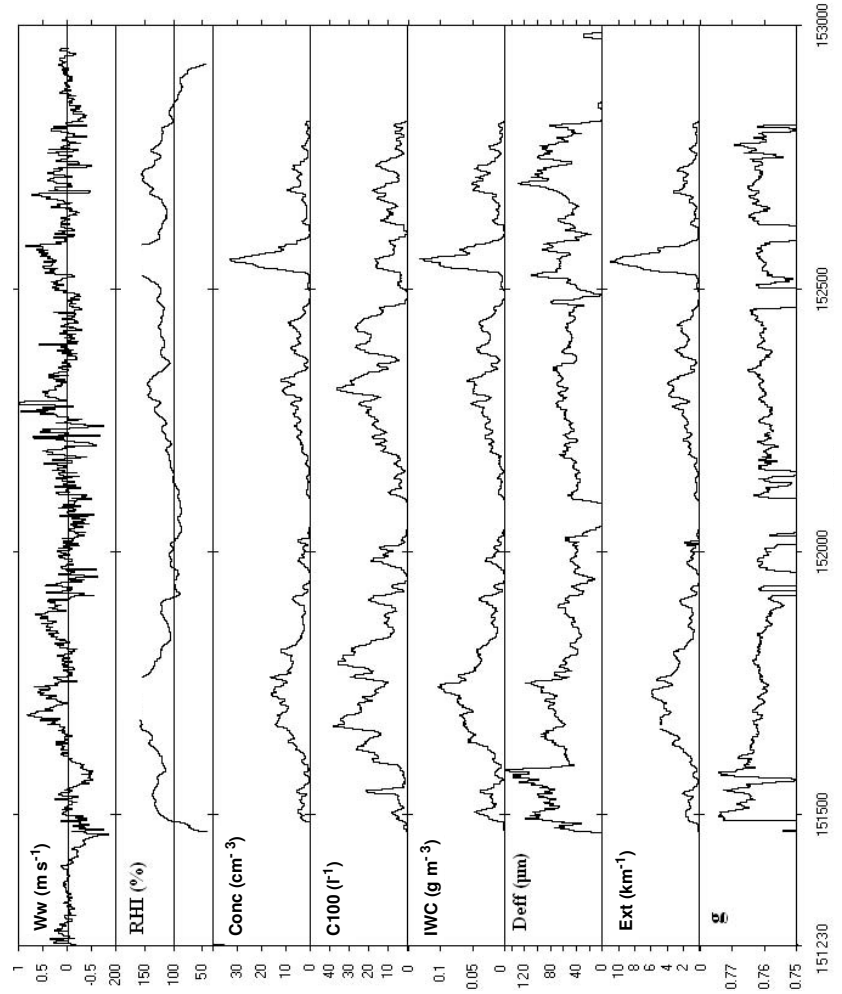

Figure 7. Time series of the parameters measured by the Falcon aircraft at 8600 m/−40 °C in the jet-stream cirrus cloud. *Ww*: vertical wind speed, *RHi*: relative humidity (with respect to ice), *Conc*: ice particle concentration, *C100*: concentration of particles ($D > 100\,\mu$m), *IWC*: ice water content, *Deff*: effective diameter, *Ext*: extinction coefficient, and *g*: asymmetry parameter.

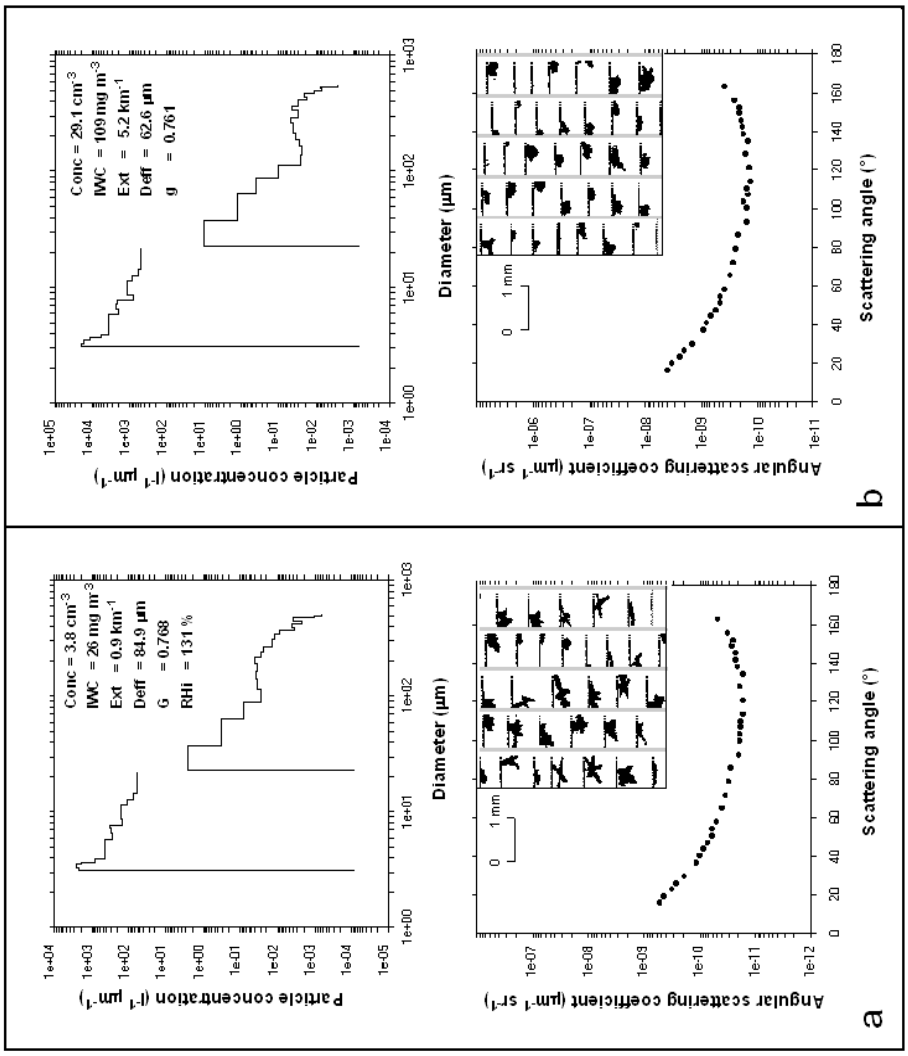

Figure 8. Upper panel: FSSP-300 and 2D-C size distributions and values of the corresponding distribution parameters. Lower panel: measured (Polar Nephelometer) and example of 2D-C images of ice crystals. (a) Example of measurements obtained between 15:15:00 and 15:15:30. (b) Example of measurements obtained between 15:25:30 and 15:25:36 UTC.

area in which the ice particles grow very rapidly because of strong supersaturation related to strong updraughts. Liquid water saturation may have been reached in the active ice-crystal generation area. However, the temporal resolution of the frost-point hygrometer makes this difficult to confirm unambiguously.

(*b*) *Wave-induced ice-cloud (flight on 13 April)*

On 13 April, following the passage of the trough the previous day, strong westerly winds throughout the troposphere advected warmer air with a higher moisture content. Backward trajectories show that some of the air was lifted from the boundary layer at 30–40°S east of Australia up to 350 hPa in the previous five days; this pattern is typical for a warm sector of a cyclone. The homogeneous wind direction led to the propagation of terrain-induced waves in the stably stratified troposphere up to the tropopause. The mountain waves induced a stagnant cirrus shield over the Punta Arenas area, which persisted for several hours from 1800 to 2400 UTC.

The orographic-wave ice-cloud was sampled at four different levels by the Falcon aircraft with a flight pattern centred near the AWI Lidar location (±20 km). Approximately 10 to 20 minutes separate the two types of measurement, and during the observation period a broken medium-thin altostratus layer sometimes obscured observation of the wave cloud above. Nevertheless, due to the quasi-stable dynamical and thermodynamical conditions which prevailed during the wave situation, comparisons between *in situ* and lidar measurements may be qualitatively assessed.

Figures 9(a) to 9(f) represent the vertical profiles of several microphysical and optical parameters as obtained by the Falcon aircraft in the cloud layers between 2010 and 2035 UTC. The cloud parameter values presented are only estimates of the actual values at the position of the lidar because of the natural cloud inhomogeneity, the cloud time-variability and the different geographical locations of the aircraft along the corresponding flight paths. Figure 9 clearly reveals two distinct and decoupled cloud layers.

The lower layer, observed between 6900 m/−29 °C and 7200 m/−33 °C, is observed to be a supercooled water altostratus cloud as the values of the asymmetry parameter (Fig. 9(f)) are high, lying between 0.800 and 0.823 (see for instance Gayet *et al.* 2002b). The presence of liquid droplets in this cloud layer is confirmed by the zero values of the depolarization ratio derived from the lidar observations (see the depolarization profile in Fig. 9(h)). This observation corresponds to the lowest temperature (−33 °C) for which supercooled water droplets were detected during the southern hemisphere INCA experiment.

The upper layer is an orographic-wave cloud observed from 8000 m/−38 °C to 9600 m/−49 °C. Contrasting with most of the previous studies (see aforementioned references), our observations relating to wave-cloud microphysics reveal only the presence of ice crystals (non-transient liquid phase was detected). Accordingly the cloud was classified as 'ice-cloud'. Figure 9(a) shows that the ice particle concentration increases from the cloud base to the mid-layer to about 60 cm^{-3} with large horizontal heterogeneities (see below) and maximum values up to 116 cm^{-3}. The mean effective diameter (Fig. 9(e)) is unusually small (about 11 μm) with fluctuations up to 25 μm at the four distinct sampling levels. The values of the asymmetry parameter (between 0.76 and 0.79, see Fig. 9(f)) prove that these small particles are definitively non-spherical and must therefore be ice particles. This is confirmed by the strong depolarization ratio (values up to 80%) derived from the lidar measurements (Fig. 9(h)). We note in passing that a ratio of 80% is much larger than the usual values observed in cirrus clouds (Sassen 1991). Multiple scattering effects due to the very dense cloud may explain the

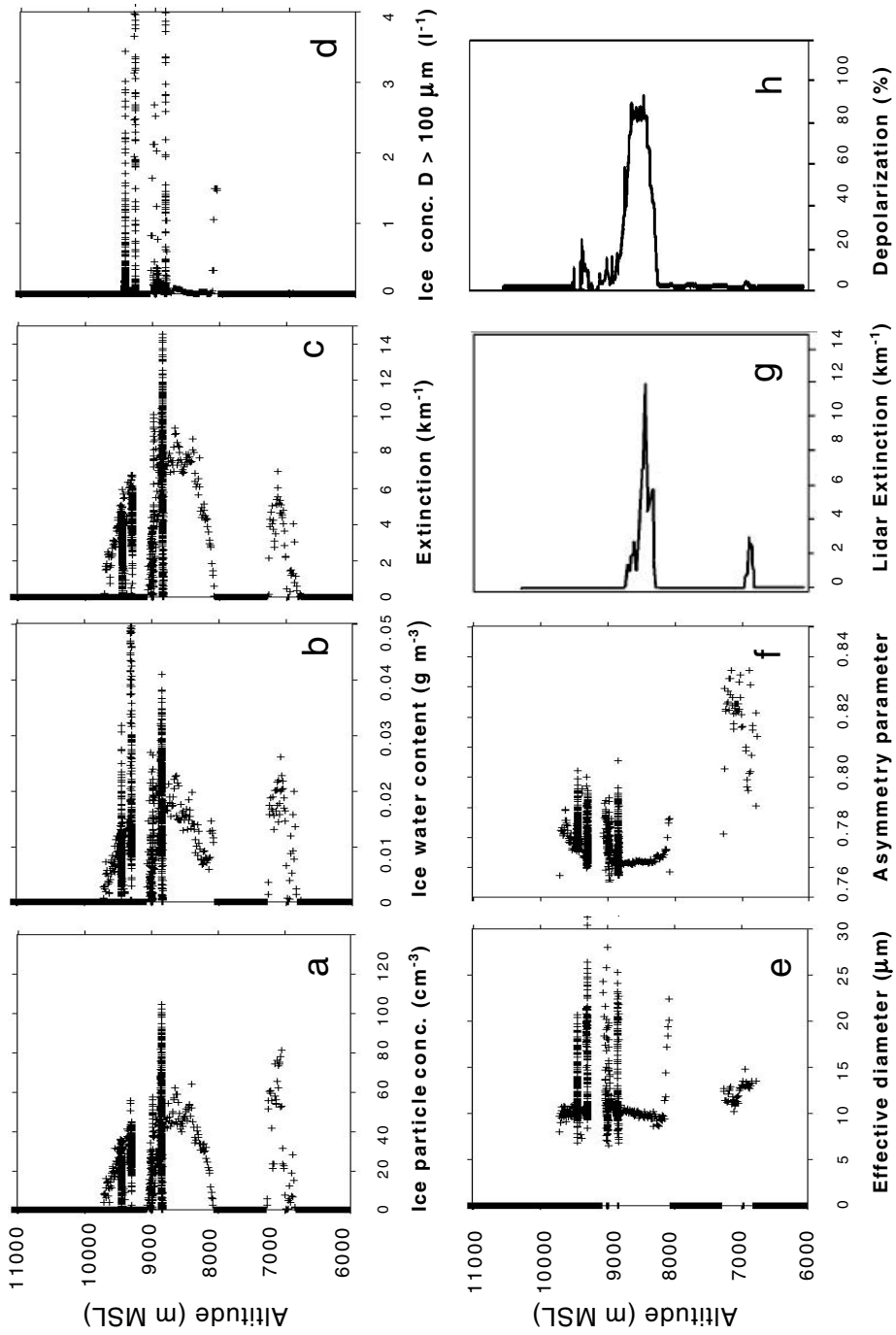

Figure 9. Microphysical and optical cloud parameters versus the altitude obtained in orographic-wave ice-cloud on 13 April: (a) ice particle concentration, (b) ice water content, (c) extinction coefficient, (d) concentration of ice particles with $D > 100$ μm, (e) effective diameter, (f) asymmetry parameter, (g) extinction derived from MARL lidar at 532 nm and (h) lidar depolarization (at 532 nm).

overestimation of the depolarization ratio. The ice water content profile (Fig. 9(b)) also reveals large fluctuations (mean and maximum values of 20 mg m^{-3} and 57 mg m^{-3} respectively), and a similar profile is observed for the extinction coefficient (Fig. 9(c)) with very high values up to 14 km^{-1}. The concentration of large ice particles ($D >$ 100 μm) peaks at 4 l^{-1} (Fig. 9(d)). The interpretation of the lidar measurements confirms the very high value of the extinction coefficient (12 km^{-1}, see Fig. 9(g)) and the colour index, which remains close to zero in most of the observed cirrus clouds but which significantly increases to about 0.8 in the wave ice-cloud (Gayet *et al.* 2002c). According to scattering theory (Liu and Mishchenko 2001), such high values indicate the presence of very small particles. Following the extinction profile on Fig. 9(c) the cloud optical depth (in the visible) may be roughly estimated as being 10. Therefore the Raman lidar could have been strongly attenuated and was probably not able to reach the cloud top as suggested by the results on Fig. 9(g).

In order to illustrate the cloud horizontal heterogeneities, Fig. 10 shows time series of the cloud parameters together with the relative humidity. These results were obtained during a 4-minute sample of the cloud at the 8800 m/−43 °C level. We recall that it was not possible to derive the vertical wind component from the Falcon measurements for this cloud sequence due to inadequately stabilized flight path length. Figure 10 shows that the aircraft sampled three distinct cloud patches with rather similar properties. Very high concentrations (up to 116 cm^{-3}) of small ice particles with a constant effective diameter ($Deff = 11$ μm) are observed within most of the cloud. The asymmetry parameter is close to constant (0.760), and the concentration of particles larger than 100 μm is very low (a few particles per litre). It may be noted in passing that the occurrence of the numerous small ice crystals cannot be due to the shattering of large ice crystals on the probe inlets, as particles larger than 50 μm were rarely detected by the 2D-C probe in these regions (Gayet *et al.* 2002a). A noteworthy observation concerns the relationship between the cloud properties and the humidity field. Outside of the cloud the air is supersaturated with *RHi* up to 130%, whereas the humidity drops to equilibrium (*RHi* of 100%) within the inner-cloud part where only small ice particles are observed. This indicates that all the available water vapour was fully consumed by the formation of numerous ice crystals offsetting their growth. This is a very different feature from the previous case where the humidity remained supersaturated within most of the in-cloud parts. Ice crystals larger than 100 μm and subsequent larger effective diameter and asymmetry parameter are detected only on the fringes of the cloud where water vapour is still available for further growth. This feature explains the large gradients in the effective diameter and the asymmetry parameter in Fig. 9.

Although the two clouds described above have formed at similar ranges of temperatures and with similar aerosol properties (see Table 2(a)), strong differences in cloud properties and humidity fields are observed. Consistent with studies of Kärcher and Ström (2003) and Haag and Kärcher (2004), this highlights the key role of the dynamical structure in controlling the formation, evolution and subsequent radiative properties of such clouds.

Figure 11 illustrates a typical example of results observed near the middle part of the cloud (at 2026 UTC, see Fig. 10). The left panel displays the FSSP-300 and 2D-C particle size distributions with the values of the distribution parameters, whereas the right panel represents the measured (Polar Nephelometer) scattering phase function and the theoretical feature which was calculated from the FSSP-300 size distribution assuming spherical particles. As is known, scattering by ice particles is considerably greater than by spherical particles at side scatter angles ranged between 80 and 120°, leading to a significantly smaller g-value (0.758). This indicates that the shape of most

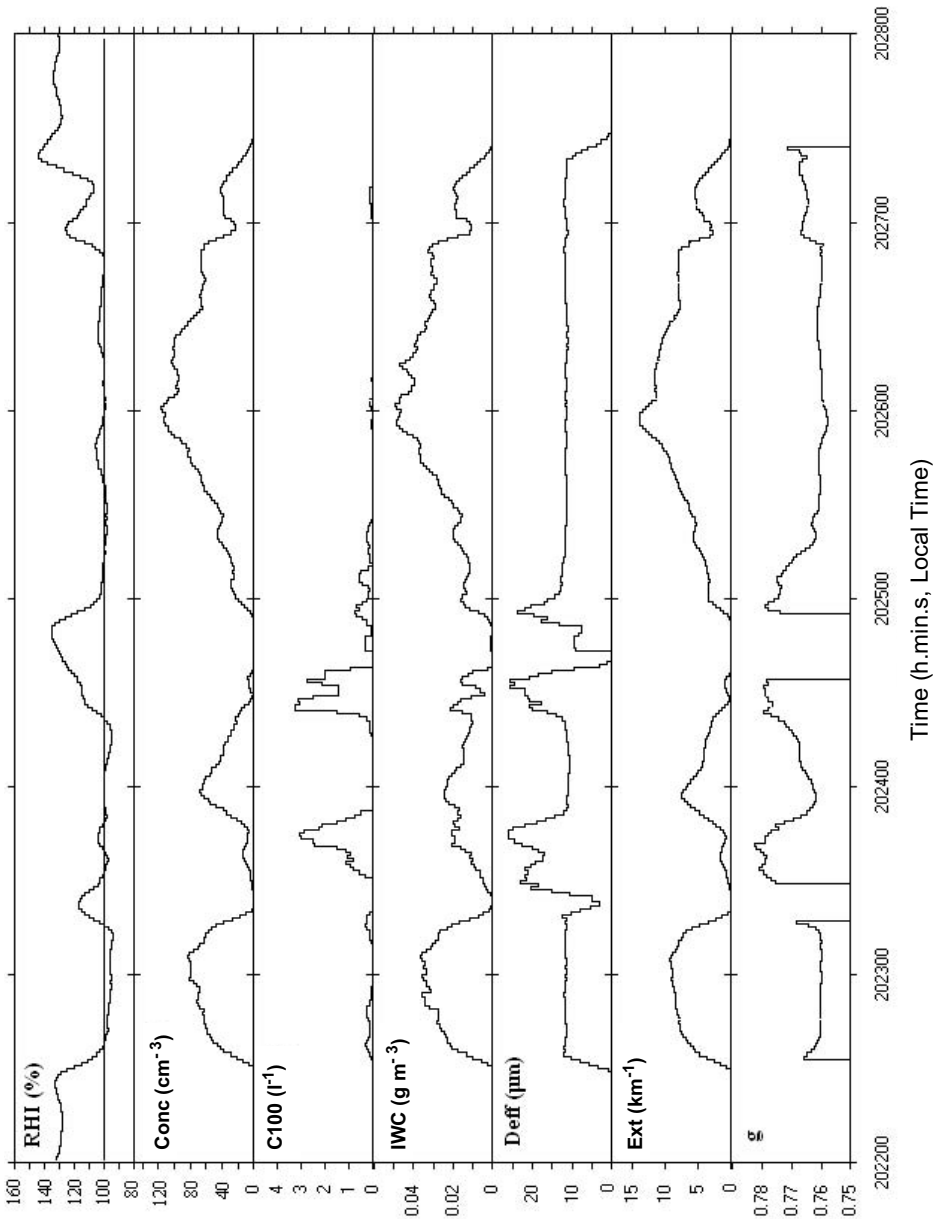

Figure 10. Time series of the parameters measured by the Falcon aircraft at 8800 m/−43 °C in the orographic-wave ice-cloud. *RHi*: relative humidity (with respect to ice), *Conc*: ice particle concentration, *C100*: concentration of particles ($D > 100$ μm), *IWC*: ice water content, *Deff*: effective diameter, *Ext*: extinction coefficient and *g*: asymmetry parameter.

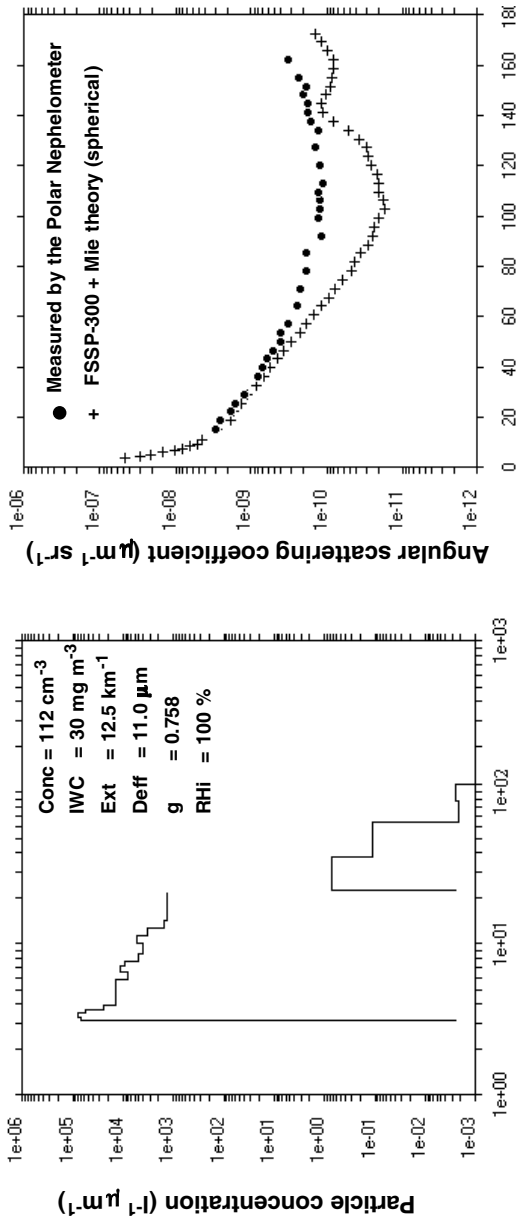

Figure 11. Example of measurements obtained at 2026 UTC. Left panel: FSSP-300 and 2D-C size distributions and values of the corresponding parameters. Right panel: measured (Polar Nephelometer) and theoretical scattering phase functions, the latter being calculated from the FSSP-300 size distribution and assuming ice spheres.

of the observed ice particles at sizes smaller than 11 μm strongly deviates from the spherical form. These particles are likely to be droxtals as observed by Zhang *et al.* (2004) in wave clouds. Similar observations were also reported by Baumgardner *et al.* (2005) but, in this instance, for larger particle sizes (30 μm). Heterogeneous nucleation cannot explain the observed high number of ice particles. Therefore the ice crystals which, it may be hypothesized, are formed by homogeneous freezing droplets, no longer maintain their original shape. From laboratory experiments, Gonda and Yamazaki (1984) found that particles become aspherical within a time scale of 10 to 20 minutes. Our findings suggest even shorter time scales.

5. Summary and conclusions

Airborne measurements of microphysical and optical properties of high-altitude clouds were performed at temperatures between $-25\,^{\circ}$C and $-62\,^{\circ}$C at midlatitudes of the southern hemisphere from Punta Arenas (53°S) in March and April 2000 during the INCA experiment.

The reliability of the PMS FSSP-300 and 2D-C measurements carried out with the high airspeed Falcon aircraft was carefully examined. The effect of crystal-shattering on FSSP measurements was evaluated and may be considered as being no greater than the usual random uncertainties. The interpretation of different measurements from a combination of four independent techniques (PMS FSSP and 2D-C, Counterflow Virtual Impactor and Polar Nephelometer) allowed inherent probe limitations to be overcome. Therefore a coherent dataset was obtained with the estimate of subsequent uncertainties on derived parameters.

The results confirm that a large fraction of the air inside most of the cirrus clouds is ice-supersaturated. Following previous INCA data interpretations, these properties may be related to cirrus cloud ice-nucleation thresholds at onset of clouds consistent with homogeneous freezing and to the action of vertical motions at various spatial and temporal scales.

Microphysical and optical properties of midlatitude cirrus clouds observed in the southern hemisphere during INCA are of the same order of magnitude as found in previous measurements (carried out mainly in the northern hemisphere) in terms both of median values and quartiles. Indeed, ice particle concentrations generally decrease with temperature, from 2.2 cm^{-3} near $-25\,^{\circ}$C to 0.5 cm^{-3} at $-60\,^{\circ}$C. As expected, the ice water content and the extinction coefficient decrease with temperature from about 18 mg m^{-3} to 0.05 mg m^{-3} and from 0.7 km^{-1} to 0.08 km^{-1}, respectively. A similar trend is observed for the effective diameter, which decreases from about 80 μm to 17 μm in the range of temperature considered. The lowest temperature at which supercooled water droplets were detected was $-33\,^{\circ}$C. The rather small variations of the asymmetry parameter highlight the fairly uniform optical properties of the cirrus clouds sampled in the considered range of temperature.

High-altitude clouds which form with rapid vertical transport, i.e. jet-stream cirrus, orographic-wave ice-clouds and cirrocumulus, are characterized by far higher values of the ice particle concentrations compared to the mean values as a whole. The results of two case-studies relating to a jet-stream cirrus and orographic-wave ice-cloud are presented in detail. Very strong moisture gradients are evidenced near the cloud poleward boundaries of the jet-stream cirrus. Dry air ($RHi \sim 30\%$) and significant downdraughts (down to -0.5 m s^{-1}) characterize the subsidence in the poleward part of the jet which resulted in the very dry conditions of a stratospheric intrusion. The cirrus contains rather

large ice crystals at the poleward edge (*Deff* between 80 μm and 140 μm) of a bullet–rosette shape and with a bimodal size distribution, whereas the middle part of the cloud belt constitutes an ice-generating area where the ice particles grow very rapidly due to strong supersaturation (which may reach values expected for homogeneous nucleation). Large values of the ice particle concentration, ice water content and extinction are measured (29 cm^{-3}, 109 mg m^{-3} and 5 km^{-1} respectively) with the observation of irregular-shaped ice crystals and some bullet–rosettes.

The orographic-wave ice-cloud exhibits a rather large concentration of small ice crystals (up to 116 cm^{-3} with an effective diameter of 11 μm). This implies unusually large extinction coefficients (up to 14 km^{-1}) which are confirmed by lidar retrievals. The available water vapour is fully consumed by the formation of the numerous ice crystals offsetting their subsequent growth. Larger ice crystals are detected only at the fringes of the cloud where water vapour is still available above ice saturation for further particle growth. This feature leads to large gradients in the asymmetry factor and effective diameter. The narrow range of the asymmetry parameter values (between 0.76 and 0.79) shows that the shape of ice particles strongly deviates from a spherical shape even for such small diameters. The ice crystals, hypothesized to form by homogeneously freezing droplets, do not maintain their original shape and are likely to be droxtals. Consequently, the transition from originally spherical particles to small aspherical crystals may be faster than previously observed in laboratory experiments.

Despite the two cirrus clouds described above being formed at a similar range of temperatures and with similar aerosol properties, the strong differences in cloud properties and humidity fields highlight the key role of the dynamical structure in controlling the formation, evolution and subsequent radiative properties of such high-altitude clouds.

ACKNOWLEDGEMENTS

This work was partially funded by the European Union contract EVK2-CT-1999-00039, by DLR within the projects PAZI and PAZI-2, and by a grant from the CNRS/PATOM committee. Thanks are due to our INCA colleagues for their helpful contribution to the experiments. We thank P. Minnis and his team from NASA Langley for support in providing satellite data and their analysis. We are very grateful to the members of the DLR who operated the Falcon aircraft during the two experiments. We acknowledge J.-F. Fournol and C. Gourbeyre (LaMP) for their technical assistance. The authors would like to give recognition to B. Kärcher (DLR), B. Guillemet and C. Duroure (LaMP) for helpful discussions. We thank K. James who reviewed the manuscript. A. Heymsfield (NCAR) and anonymous reviewers made important comments that strengthened the manuscript.

REFERENCES

Arnott, W. P., Dong, Y. Y., Hallett, J. and Poellot, M. R. 1994 Role of small ice crystals in radiative properties of cirrus: A case study, FIRE II, November 22, 1991. *J. Geophys. Res.*, **99,** 1371–1381

Auriol, F., Gayet, J.-F., Febvre, G., Jourdan, O., Labonnote, L. and Brogniez, G. 2001 In situ observation of cirrus scattering phase functions with 22° and 46° halos: Cloud field study on 19 February 1998. *J. Atmos. Sci.*, **58,** 3376–3390

Baker, B. A. and Lawson, R. P. 2006 In situ observations of the microphysical properties of wave, cirrus and anvil clouds. Part I: Wave clouds. *J. Atmos. Sci.*, in press

Baumgardner, D. and Korolev, A. 1997 Airspeed corrections for optical array probe sample volumes. *J. Atmos. Oceanic Technol.*, **14,** 1224–1229

Baumgardner, D., Dye, J. E., Gandrud, B. W. and Knollenberg, R. G. 1992 Interpretation of measurements made by the Forward Scattering Spectrometer Probe (FSSP-300) during the Airborne Arctic Stratosphere Expedition. *J. Geophys. Res.*, **97,** 8035–8046

Baumgardner, D., Chepfer, H., Raga, G. B. and Kok, G. L. 2005 The shapes of very small cirrus particles derived from in situ measurements. *Geophys. Res. Lett.*, **32,** doi: 10.1029/2004GL021300

Bögel, W. and Baumann, R. 1991 Test and calibration of the DLR Falcon wind measuring system by maneuvers, *J. Atmos. Oceanic Technol.*, **8,** 5–18

Boudala, F. S., Isaac, G. A., Fu, Q. and Cober, S. G. 2002 Parameterization of effective ice particle size for high-latitude clouds. *Int. J. Climatol.*, **22,** 1267–1284

Dowling, D. R. and Radke, L. F. 1990 A summary of the physical properties of cirrus clouds. *J. Appl. Meteorol.*, **29,** 970–978

Field, P. R., Cotton, R. J., Noone, K., Glantz, P., Kaye, P. H., Hirst, E., Greenaway, R. S., Jost, C., Gabriel, R., Reiner, T., Andreae, M., Saunders, C. P. R., Archer, A., Choularton, T., Smith, M., Brooks, B., Hoell, C., Bandy, B., Johnson, D. and Heymsfield, A. J. 2001 Ice nucleation in orographic wave clouds: Measurements made during INTACC. *Q. J. R. Meteorol. Soc.*, **127,** 1493–1512

Field, P. R., Wood, R., Brown, P. R. A., Kaye, P. H., Hirst, E., Greenaway, R. and Smith, J. 2003 Ice particle interarrival times measured with a Fast FSSP. *J. Atmos. Oceanic Technol.*, **20,** 249–261

Francis, P. N., Hignett, P. and Macke, A. 1998 The retrieval of cirrus cloud properties from aircraft multi-spectral reflectance measurements during EUCREX'93. *Q. J. R. Meteorol. Soc.*, **124,** 1273–1291

Gallagher, M. W., Connolly, P. J., Whiteway, J., Figueras-Nieto, D., Flynn, M., Choularton, T. W., Bower, K. N., Cook, C., Busen, R. and Hacker, J. 2005 An overview of the microphysical structure of cirrus clouds observed during EMERALD-1. *Q. J. R. Meteorol. Soc.*, **131,** 1143–1169

Gayet, J.-F., Crépel, O., Fournol, J.-F. and Oshchepkov, S. 1997 A new airborne Polar Nephelometer for the measurements of optical and microphysical cloud properties. Part I: Theoretical design. *Annales Geophysicae*, **15,** 451–459

Gayet, J.-F., Auriol, F., Oshchepkov, S., Schröder, F., Duroure, C., Febvre, G., Fournol, J.-F., Crépel, O., Personne, P. and Daugereon, D. 1998 In situ measurements of the scattering phase function of stratocumulus, contrails and cirrus. *Geophys. Res. Lett.*, **25,** 971–974

Gayet, J.-F., Auriol, F., Minikin, A., Ström, J., Seifert, M., Krejci, R., Petzold, A., Febvre, G. and Schumann, U. 2002a Quantitative measurement of the microphysical and optical properties of cirrus clouds with four different in situ probes: Evidence of small ice crystals. *Geophys. Res. Lett.*, **29,** 2230, doi: 10.1029/2001GL014342

Gayet, J.-F., Asano, S., Yamazaki, A., Uchiyama, A., Sinyuk, A., Jourdan, O. and Auriol, F. 2002b Two case studies of winter continental-type water and mixed-phase stratocumuli over the sea. 1: Microphysical and optical properties. *J. Geophys. Res.*, **107,** 4569, doi: 10.1029/2001JD001106

Gayet, J.-F., Immler, F., Auriol, F., Minikin, A., Petzold, A., Ovarlez, J. and Ström, J. 2002c 'Microphysical and optical properties of a wave-cirrus cloud sampled during the INCA experiment'. Proc. 11th AMS conference on Cloud Physics, 3–7 June 2002, Ogden, Utah, USA

Gayet, J.-F., Ovarlez, J., Shcherbakov, V., Ström, J., Schumann, U., Minikin, A., Auriol, F., Petzold, A. and Monier, M. 2004 Cirrus cloud microphysical and optical properties at southern and northern midlatitudes during the INCA experiment. *J. Geophys. Res.*, **109,** D20206, doi: 10.1029/2004JD004803

Gonda, S. and Yamazaki, T. 1984 Initial forms of snow crystals growing from frozen cloud droplets. *J. Meteorol. Soc. Jpn*, **62,** 190–192

Haag, W. and Kärcher, B. 2004 The impact of aerosols and gravity waves on cirrus clouds at midlatitudes. *J. Geophys. Res.*, **109,** D12202, doi: 10.1029/2004JD004579

Haag, W., Kärcher, B., Ström, J., Minikin, A., Lohmann, U., Ovarlez, J. and Stohl, A. 2003 Freezing thresholds and cirrus cloud formation mechanisms inferred from in situ measurements of relative humidity. *Atmos. Chem. Phys.*, **3,** 1791–1806

Haynes, J. M. and Stephens, G. L. 2002 'A composite and microphysical study of jet stream cirrus over the ARM site'. Twelfth ARM Science Team Meeting Proceedings, St Petersburg, Florida, 8–12 April 2002

Heymsfield, A. J. 1972 Ice crystal terminal velocities. *J. Atmos. Sci.*, **29,** 1348–1357

1993 Microphysical structure of stratiform and cirrus clouds. Pp. 97–121 in *Aerosol-cloud-climate interactions*. Ed. P. V. Hobbs. Academic Press

Heymsfield, A. J. and Donner, L. J. 1990 A scheme for parameterizing ice-cloud water content in general circulation models. *J. Atmos. Sci.*, **47,** 1865–1877

Heymsfield, A. J. and McFarquhar, G. M. 2002 Mid-latitude and tropical cirrus: Microphysical properties. Pp. 78–101 in *Cirrus*. Eds. D. K. Lynch, K. Sassen, D. O'C. Starr and G. Stephen. Oxford University Press, New York

Heymsfield, A. J. and Miloshevich, L. M. 1993 Homogeneous ice nucleation and supercooled liquid water in orographic wave clouds. *J. Atmos. Sci.*, **50,** 2335–2353

1995 Relative humidity and temperature influences on cirrus formation and evolution: Observations from wave clouds in FIRE II. *J. Atmos. Sci.*, **52,** 4302–4326

Heymsfield, A. J. and Parrish, J. L. 1978 A computational technique for increasing the effective sampling volume of the PMS two-dimensional particle size spectrometer. *J. Appl. Meteorol.*, **17,** 1566–1572

Heymsfield, A. J., Miller, K. M. and Spinhirne, J. D. 1990 The 27–28 October 1986 FIRE IFO cirrus case study: Cloud microstructure. *Mon. Weather Rev.*, **118,** 2313–2328

Immler, F. and Schrems, O. 2002 LIDAR measurements of cirrus clouds in the northern and southern midlatitudes during INCA (55°N, 53°S): A comparative study. *Geophys. Res. Lett.*, **29,** 1809, doi: 10.1029/2002GL015077

Kärcher, B. and Lohmann, U. 2002 A parameterization of cirrus cloud formation: Homogeneous freezing including effects of aerosol size. *J. Geophys. Res.*, **107,** 4698, doi: 10.1029/2001JD001429

Kärcher, B. and Ström, J. 2003 The roles of dynamical variability and aerosols in cirrus cloud formation. *Atmos. Chem. Phys.*, **3,** 823–838

Kärcher, B., Hendricks, J. and Lohmann, U. 2006 Physically based parameterization of cirrus cloud formation for use in global atmospheric models. *J. Geophys. Res.*, **111,** D01205, doi: 10.1029/2005JD006219

Khvorostyanov, V. I. and Sassen, K. 1998 Cirrus cloud simulation using explicit microphysics and radiation. Part II: Microphysics, vapor and ice mass budgets, and optical and radiative properties. *J. Atmos. Sci.*, **55,** 1822–1845

Koop, T., Luo, B. P., Tsias, A. and Peter, T. 2000 Water activity as the determinant for homogeneous ice nucleation in aqueous solutions. *Nature*, **406,** 611–614

Lawson, R. P., Heymsfield, A. J., Aulenbach, S. M. and Jensen, T. L. 1998 Shapes, sizes and light scattering properties of ice crystals in cirrus and a persistent contrail during SUCCESS. *Geophys. Res. Lett.*, **25,** 1331–1334

Lawson, R. P., O'Connor, D., Zmarzly, P., Weaver, K., Baker, B., Mo, Q. and Jonsson, H. 2006a The 2D-S (Stereo) probe: Design and preliminary tests of a new airborne, high-speed, high-resolution particle imaging probe. *J. Atmos. Oceanic Technol.*, in press

Lawson, R. P., Baker, B., Pilson, B. and Mo, Q. 2006b In situ observations of the microphysical properties of wave, cirrus and anvil clouds. Part II: Cirrus clouds. *J. Atmos. Sci.*, in press

Liou, K.-N. 1986 Influence of cirrus clouds on weather and climate processes: A global perspective. *Mon. Weather Rev.*, **114,** 1167–1199

Liu, L. and Mishchenko, M. I. 2001 Constraints on PSC particle microphysics derived from lidar observations. *J. Quant. Spectrosc. Radiat. Transfer*, **70,** 817–831

Locatelli, J. D. and Hobbs, P. V. 1974 Fall speeds and masses of solid precipitation particles. *J. Geophys. Res.*, **79,** 2185–2197

Minikin, A., Petzold, A., Ström, J., Krejci, R., Seifert, M., Schlager, H., van Velthoven, P. and Schumann, U. 2003 Aircraft observations of the upper tropospheric fine particle aerosol in the northern and southern hemispheres at midlatitudes. *Geophys. Res. Lett.*, **30,** 1503, doi: 10.1029/2002GL016458

Noone, K. J., Ogran, J. A., Heintzenberg, J., Charlson, R. J. and Covert, D. S. 1993 Design and calibration of a counterflow virtual impactor for sampling of atmospheric fog and cloud droplets, *Aerosol Sci. Technol.*, **8,** 235–244

Ovarlez, J., van Velthoven, P., Sachse, G., Vay, S., Schlager, H. and Ovarlez, H. 2000 Comparison of water vapor measurements from POLINAT2 with ECMWF analyses in high-humidity conditions. *J. Geophys. Res.*, **105,** 3737–3744

Ovarlez, J., Gayet, J.-F., Gierens, K., Ström, J., Ovarlez, H., Auriol, F., Busen, R. and Schumann, U. 2002 Water vapour measurements inside cirrus clouds in northern and southern hemispheres during INCA. *Geophys. Res. Lett.*, **29,** doi: 10.1029/2001GL014440

Raschke, E., Schmetz, J., Heintzenberg, J., Kandel, R. and Saunders, R. 1990 International Cirrus Experiment (ICE). A joint European effort. *Eur. Space Agency J.*, **14,** 193–199

Rossow, W. B. and Schiffer, R. A. 1999 Advances in understanding clouds from ISCCP. *Bull. Am. Meteorol. Soc.*, **80,** 2261–2287

Sassen, K. 1991 The polarization lidar technique for cloud research: A review and current assessment. *Bull. Am. Meteorol. Soc.*, **72,** 1848–1866

2002 Cirrus cloud: A modern perspective. Pp. 11–40 in *Cirrus*. Eds. D. K. Lynch, K. Sassen, D. O'C. Starr, G. Stephen. Oxford University Press, New York

Sassen, K., Starr, D. O'C., Mace, G. G., Poellot, M. R., Melfi, S. H., Eberhard, W. L., Spinhirne, J. D., Eloranta, E. W., Hagen, D. E. and Hallett, J. 1995 The 5–6 December 1991 FIRE IFO II jet stream cirrus case study: Possible influences of volcanic aerosols. *J. Atmos. Sci.*, **52,** 97–123

Sauvage, L., Chepfer, H., Trouillet, V., Flamant, P. H., Brogniez, G., Pelon, J. and Albers, F. 1999 Remote sensing of cirrus radiative properties during EUCREX'94. Case study of 17 April 1994. Part 1: Observations. *Mon. Weather Rev.*, **127,** 486–503

Schröder, F., Kärcher, B., Duroure, C., Ström, J., Petzold, A., Gayet, J.-F., Strauss, B., Wendling, P. and Borrmann, S. 2000 On the transition of contrails into cirrus clouds. *J. Atmos. Sci.*, **57,** 464–480

Seifert, M., Ström, J., Krejci, R., Minikin, A., Petzold, A., Gayet, J.-F., Schumann, U. and Ovarlez, J. 2003 In-situ observations of aerosol particles remaining from evaporated cirrus crystals: Comparing clean and polluted air masses. *Atmos. Chem. Phys.*, **3,** 1037–1049

Seifert, M., Ström, J., Krejci, R., Minikin, A., Petzold, A., Gayet, J.-F., Schlager, H., Ziereis, H., Schumann, U. and Ovarlez, J. 2004 Aerosol–cirrus interactions: A number based phenomenon at all? *Atmos. Chem. Phys.*, **4,** 293–305

Shcherbakov, V., Gayet, J.-F., Jourdan, O., Minikin, A., Ström, J. and Petzold, A. 2005 Assessment of cirrus cloud optical and microphysical data reliability by applying statistical procedures. *J. Atmos. Oceanic. Technol.*, **22,** 409–420

Strapp, J. W., Albers, F., Reuter, A., Korolev, A. V., Maixner, U., Rashke, E. and Vukovic, Z. 2001 Laboratory measurements of the response of a PMS OAP-2DC. *J. Atmos. Oceanic Technol.*, **18,** 1150–1170

Ström, J., Schumann, U., Gayet, J.-F., Ovarlez, J., Flatoy, F., Kulmala, M., Schrems, O., Minnis, P., Diaz, S. B., Milicic, B., Valderama, V., Amthauer, E., Pettersson, J. and Arnold, F. 2001 Aerosol and cirrus measurements at midlatitudes on the southern hemisphere: An overview based on the first INCA experiment. *Air Pollut. Rep.*, **74,** Report EUR 19428 EN, European Commission, Brussels

Ström, J., Seifert, M., Ovarlez, J., Minikin, A., Gayet, J.-F., Krejci, R., Petzold, A., Auriol, F., Busen, R., Schumann, U., Kärcher, B., Haag, W. and Hansson, H.-C. 2003 Cirrus cloud occurrence as function of ambient relative humidity: A comparison of observations obtained during the INCA experiment. *Atmos. Chem. Phys.*, **3,** 1807–1816

Wylie, D. P. and Menzel, W. P. 1999 Eight years of high cloud statistics using HIRS. *J. Climate*, **12,** 170–184

Zhang, Z., Yang, P., Kattawar, G. W., Tsay, S.-C., Baum, B. A., Hu, Y., Heymsfield, A. J. and Reichardt, J. 2004 Geometrical-optics solution to light scattering by droxtal ice crystals. *Appl. Opt.*, **43,** 2490–2499